AGU ADVANCING EARTH AND SPACE SCIENCES

Tectonics®

RESEARCH ARTICLE
10.1029/2023TC007748

Lower Crustal Rheology Controls Strain Partitioning and Mode of Intracontinental Deformation

Xi Xu[1,2,3], Andrew V. Zuza[4], An Yin[2], Peng Yu[5], Zhiyong Chen[6], Chongjin Zhao[5], Baodi Wang[1], Hanlin Chen[3], Xiubin Lin[3], Lei Wu[3], Xingtao Kuang[1], Hefeng Tian[3], Qihang Yin[3], and Shufeng Yang[3]

[1]China Aero Geophysical Survey and Remote Sensing Center for Natural Resources, China Geological Survey, Beijing, China, [2]Department of Earth, Planetary, and Space Sciences, University of California-Los Angeles, Los Angeles, CA, USA, [3]School of Earth Sciences, Zhejiang University, Hangzhou, China, [4]Nevada Bureau of Mines and Geology, University of Nevada, Reno, NV, USA, [5]School of Ocean and Earth Science, Tongji University, Shanghai, China, [6]Research Institute of Petroleum Exploration and Development, PetroChina, Beijing, China

Key Points:

- Crustal deformation around the Tarim Basin is uniquely partitioned into predominately strike-slip faults in the east and distributed fold-thrust belts in the west
- Lower crustal viscosity impacts crust-scale deformation and strain partitioning in an intraplate setting
- Plume-driven crustal modification exerts a strong control on later continental tectonic process

Supporting Information:

Supporting Information may be found in the online version of this article.

Correspondence to:

H. Chen, B. Wang and X. Xu,
hlchen@zju.edu.cn;
baodiwang@163.com;
lexus.phd@gmail.com;
winbreak@163.com

Citation:

Xu, X., Zuza, A. V., Yin, A., Yu, P., Chen, Z., Zhao, C., et al. (2023). Lower crustal rheology controls strain partitioning and mode of intracontinental deformation. *Tectonics*, *42*, e2023TC007748. https://doi.org/10.1029/2023TC007748

Received 9 JAN 2023
Accepted 25 JUN 2023

Author Contributions:

Conceptualization: Xi Xu
Data curation: Xi Xu, Zhiyong Chen, Baodi Wang, Hanlin Chen
Formal analysis: Xi Xu, Andrew V. Zuza, An Yin, Peng Yu, Zhiyong Chen, Chongjin Zhao, Baodi Wang, Xiubin Lin, Lei Wu, Xingtao Kuang
Funding acquisition: Xi Xu, Baodi Wang, Hanlin Chen, Shufeng Yang
Investigation: Xi Xu, Andrew V. Zuza, An Yin
Methodology: Xi Xu, Andrew V. Zuza, An Yin, Peng Yu, Chongjin Zhao, Xingtao Kuang
Project Administration: Baodi Wang, Hanlin Chen, Shufeng Yang
Resources: Xi Xu, Peng Yu, Zhiyong Chen, Baodi Wang, Hanlin Chen

Abstract The factors that control strain partitioning along plate boundaries and within continental interiors remains poorly resolved. Plate convergence may be accommodated via distributed crustal shortening or discrete crustal-scale strike-slip faulting, but what controls these differing modes of deformation is debated. Here we address this question by examining the actively deforming regions that surround the Tarim Basin in central Asia, where deformation is uniquely partitioned into predominately strike-slip faults in the east and distributed fold-thrust belts in the west to accommodate Cenozoic India-Asia plate convergence. We present integrated geological and geophysical observations to elucidate patterns in crustal deformation and compositional structure in and around the Tarim Basin. The thrust-dominated western Tarim Basin correlates with a strongly-magnetic lower crust, whereas strike-slip faulting along the eastern margins of the Tarim Basin lack such magnetic signals. We suggest that the lower crust of the western Tarim is more mafic and stronger than in the east, which impacts intra-plate strain partitioning. A stronger lower crust results in vertical decoupling to drive mid-crust horizontal detachments and facilitate thrust faulting, whereas a more homogenized crust favored vertical transcrustal strike-slip faulting. These rheological differences likely originated from the impingement of the Permian Tarim plume focused in the west. A comparison with the Longmen Shan of eastern Tibetan Plateau reveals remarkably similar strain partitioning that correlates with variations in foreland rheology. Our results highlight how variations in lower-crust viscosity impact strain partitioning in an intra-plate setting and how plume processes exert a strong control on later continental tectonic processes.

Plain Language Summary Crustal deformation propagates far into the continental plate interior when continental plates collide and converge. Sometimes intra-plate deformation is expressed via distributed crustal shortening in fold-thrust belts and sometimes it is manifested as discrete vertical strike-slip faults that accommodate lateral plate motion. It remains unclear what dictates which mode of deformation operates within the continental interior. Here we examined the patterns and compositional structure of deformational belts around the Tarim Basin in central Asia using integrated geological and geophysical datasets. The western Tarim Basin is characterized by distributed shortening and the eastern basin is characterized by strike-slip faulting, and these differences correlate strength variations in the lower crust imaged via magnetic surveys and inversions. Specifically, we hypothesize the stronger crust of the western Tarim Basin allows the upper crust to detach to develop fold-thrust belts, whereas the eastern Tarim Basin has a more homogenously strong crustal column that is cut by vertical strike-slip faults. Our proposed model with lower-crust rheology controlling the mode of intra-plate deformation may be broadly applicable to zones of continental deformation.

1. Introduction

Continental convergence at plate boundaries often results in wide distributed zones of intracontinental deformation (e.g., Bendick & Flesch, 2007; Burchfiel et al., 1989; Molnar & Tapponnier, 1975; Yin, 2010). The distinct differences of continental tectonics versus rigid plate tectonics are at least in part caused by the weakness of quartz-rich continental crust compared with the oceanic lithosphere and the prevalence of intracrustal detachments within the crust due to a differentiated, heterogenous crust (e.g., W. P. Chen & Molnar, 1983; Mouthereau et al., 2013). However, whether continental convergence at plate boundaries is accommodated by distributed

Software: Peng Yu, Zhiyong Chen, Chongjin Zhao, Xingtao Kuang
Supervision: Baodi Wang, Hanlin Chen, Shufeng Yang
Validation: Andrew V. Zuza, An Yin, Baodi Wang, Hanlin Chen
Visualization: Xi Xu, Peng Yu, Chongjin Zhao, Lei Wu, Xingtao Kuang, Hefeng Tian, Qihang Yin
Writing – original draft: Xi Xu, Andrew V. Zuza
Writing – review & editing: Xi Xu, Andrew V. Zuza, An Yin, Peng Yu, Zhiyong Chen, Chongjin Zhao, Baodi Wang, Hanlin Chen, Xiubin Lin, Lei Wu, Xingtao Kuang, Hefeng Tian, Qihang Yin, Shufeng Yang

crustal shortening that can be approximated as a deforming continuum (England and Houseman, 1986; Yin & Taylor, 2011) or strike-slip displacement of smaller relatively rigid plates remains debated (e.g., Avouac & Tapponnier, 1993; Meade & Hager, 2005).

There are many deforming intra-plate regions, including the Longmen Shan in the eastern Tibetan plateau (e.g., Jiang et al., 2019; Murphy et al., 2014; Yin, 2010), the northwest Himalaya and the Karakorum fault systems (e.g., Avouac & Tapponnier, 1993; Brown et al., 2002), the Zagros (e.g., Authemayou et al., 2006) and the Tarim Basin northwest of the Tibetan plateau (e.g., Avouac & Tapponnier, 1993; Bendick et al., 2000; Cowgill et al., 2003; Laborde et al., 2019), that all exhibit variable partitioning between distributed crustal shortening and discrete strike-slip faulting. Deciphering the controls on these differing styles of deformation can inform us about modes of continental tectonics. To address these issues, we specifically examined the styles of continental deformation around the Tarim Basin in central Asia (Figure 1), where deformation is variably but almost equally divided between crustal shortening and strike-slip faulting.

The Tarim Basin is one of the most prominent features of the Cenozoic Himalayan-Tibetan orogen (Molnar & Tapponnier, 1975; Yin, 2010). Enclosed by the highly-deformed Tibetan plateau and Tian Shan, the interior of the Tarim Basin lithosphere experienced relatively minimal Cenozoic deformation and it resisted northward expansion of the plateau (England and Houseman, 1986; Yin & Harrison, 2000). However, the mountain ranges surrounding the Tarim Basin are strongly deformed, including significant crustal shortening in the Pamir and Tian Shan in the west and strike-slip faulting in the east (e.g., Laborde et al., 2019; Yin et al., 1998) (Figure 1). These different deformational modes may be caused by lithospheric strength variations (e.g., Calignano et al., 2015; L. Chen et al., 2017; Mouthereau et al., 2013), intracrustal detachments between the upper and lower crust (e.g., Burchfiel et al., 1989; Royden, 1996) within the converging plates due to unique geologic histories, or differences in lateral boundary conditions around central Asia (e.g., Schellart et al., 2019; Tapponnier et al., 1982; Yin, 2010).

The high-relief mountain ranges surrounding the Tarim Basin do not exhibit significant pre-Cenozoic differences along strike (e.g., Yin & Harrison, 2000). Therefore, we investigated the composition and structure of the Tarim Basin as it potentially relates to driving different styles of deformation around its periphery (e.g., Mouthereau et al., 2013). The Tarim Basin consists of ~10 km Mesozoic–Cenozoic strata that cover its older geologic history (Guo et al., 2005), which thus necessitates geophysical methods to probe its underlying bedrock. Aeromagnetic and seismic-reflection imaging have proven to be effective tools for estimating crustal composition and deformation (e.g., Laborde et al., 2019; Saltus et al., 2006), and here we report high-resolution crust-scale geophysical datasets to constrain patterns of deformation in and around the Tarim Basin. By evaluating these data in conjunction with published geological and geophysical observations from the Tarim Basin and its surrounding mountain belts, we propose a unifying model for crust-scale strain propagation and partitioning during the convergence of stiff craton-like continents and weaker deformable continents. Our work provides new insights into fault development in collisional settings, and how the mid-lower crustal rheology controls the deformation mode along the margins of Tibetan Plateau.

2. Tectonic Setting

The Tarim Basin in central Asia is a ~700-km-wide and ~1,500-km-long endorheic sedimentary basin with an average elevation of ~1.2 km (Figure 1a). The Tarim Basin is a relatively rigid, minimally deformed lithospheric block nested within Cenozoic Himalayan-Tibetan orogen (Molnar & Tapponnier, 1975; Yin & Harrison, 2000), flanked by strongly-deformed orogenic belts, including the Tibetan plateau to the southeast, the Pamir to southwest, and the Tian Shan to the north, as well as widespread strike-slip fault systems such as the left-slip Altyn Tagh fault (ATF) (Cowgill et al., 2003; Yin et al., 2002). Proterozoic crystalline basement terranes within the basin (Deng et al., 2017; Z. Xu et al., 2013; P. Zhao et al., 2021) are overlain by Neoproterozoic to Phanerozoic sedimentary cover (e.g., Guo et al., 2005; Zhang et al., 2013). The North and South Tarim continents collided in the Neoproterozoic along a presently west-trending suture zone that traverses the Tarim Basin (Guo et al., 2005; Wen et al., 2018; H. Yang et al., 2018; P. Zhao et al., 2021). The Neoproterozoic suture zone was reactivated during early Paleozoic orogeny (Carroll et al., 2001; Guo et al., 2005) that impacted much of the northern Tibet region (e.g., C. Wu et al., 2016; Zuza & Yin, 2017; Zuza et al., 2018). The Tarim continent was thus weak and deformable until at least the early Paleozoic, which suggests that it was strengthened to become a rigid, craton-like continent between the early Paleozoic and Cenozoic.

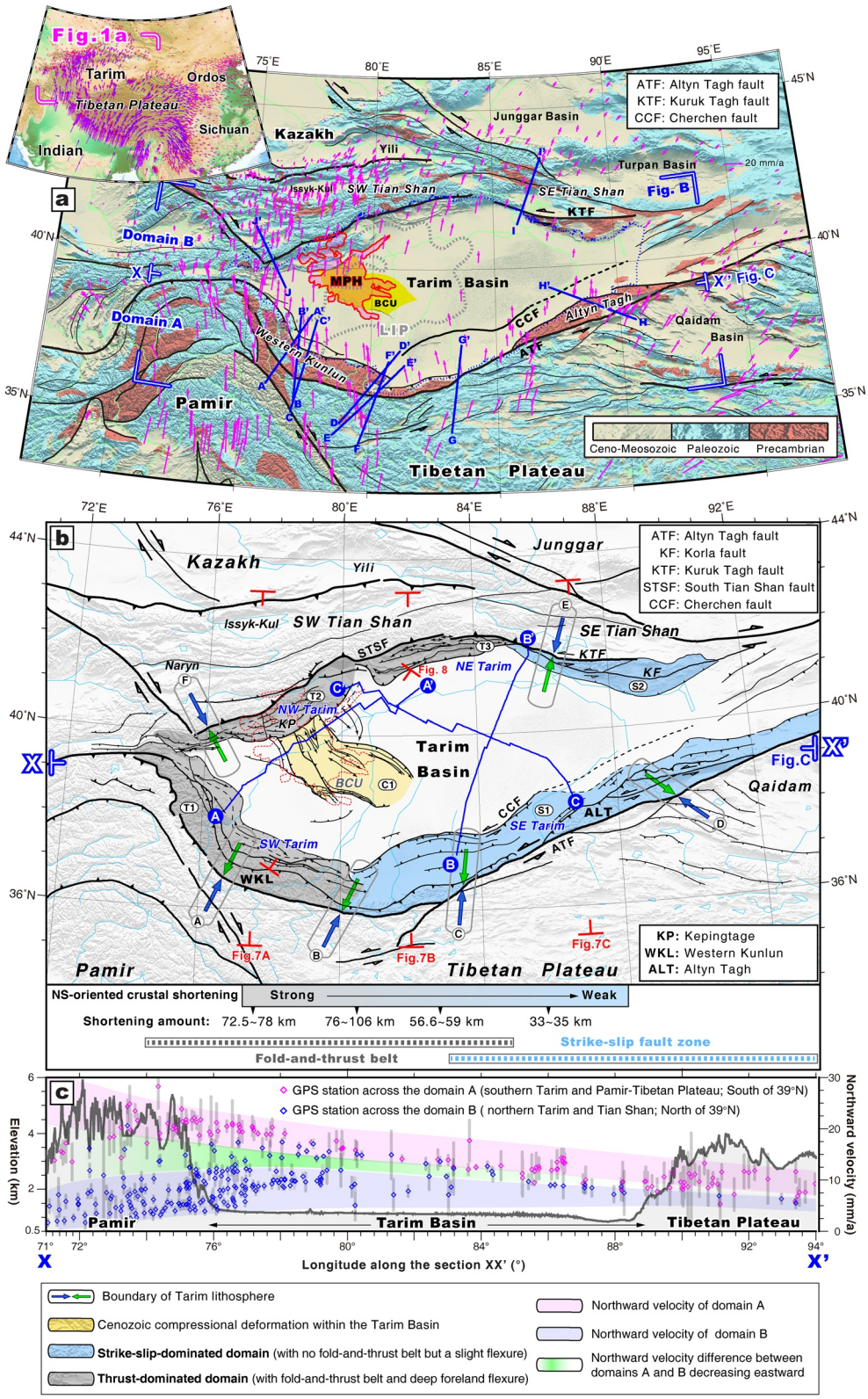

Figure 1.

The modern Tarim Basin has low heat flow (S. Liu et al., 2015), low topographic relief (Calignano et al., 2015), and experienced negligible Cenozoic deformation across the basin with flat-lying and largely undeformed Cenozoic sedimentary strata (e.g., Guo et al., 2005). Although a transmogrification mechanism (Morgan & Vannucchi, 2022) would alternatively convert buried oceanic lithosphere (Kusky & Mooney, 2015) into continental lithosphere, based on this geologic history, and the observation of a voluminous Permian large-igneous province (e.g., S. Yang et al., 2013), it has been interpreted that the Tarim continental block was welded to be a rigid craton-like continent by Permian plume impingement across the western Tarim domain (X. Xu et al., 2023). This process ultimately thickened the Tarim lithosphere to its present-day thickness of ∼200-km (Y. Xu et al., 2002).

The main orogenic regions around the Tarim Basin include the Tibetan plateau to the southeast, Pamir and Western Kunlun Range to the southwest, and Tian Shan to the north. The Tibetan plateau region consists of a series of roughly west-trending terranes including Qilian, Qaidam, Songpan-Ganzi, Qiangtang, and Lhasa blocks that were accreted to the southern margin of the Eurasian continent during multistage arc-continent collision during Phanerozoic (C. Wu et al., 2016; Xiao et al., 2013; Yin & Harrison, 2000). The Tian Shan orogenic belt formed as a result of the Paleozoic accretion of island arcs and microcontinents to the Eurasian margin, associated closing of the Paleo-Asian Ocean, and the final collision between Tarim and Eurasia (Windley et al., 1990; Xiao et al., 2013; Zuza & Yin, 2017).

Well-documented Cenozoic deformation in and around the Tarim Basin region illustrate a pronounced west-to-east difference in styles and rates of intracontinental crustal shortening (Figure 1; Laborde et al., 2019). To the west, ∼49–83-km of crustal shortening was accommodated across the contractional Western Kunlun and southwestern Tian Shan ranges, whereas ∼15–44-km of shortening was accommodated across the transpressional Altyn Tagh and southeastern Tian Shan ranges (Laborde et al., 2019). Geodesy demonstrates a similar decrease in north-south convergence because the western portion of the Tarim Basin convergences with Eurasia at a rate of 20 ± 5 mm/year, whereas the eastern part convergences at 10 ± 5 mm/year (Zheng et al., 2017) (Figure 1c and Figure S2 in Supporting Information S1).

The ∼2,000-km-long Altyn Tagh left-slip fault bounds the northwest margin of the Tibetan plateau, separating it from the Tarim Basin (e.g., Bendick et al., 2000; Cowgill et al., 2003; Yin et al., 2002). The ATF accommodates the relative motion between Tibet and the Tarim Basin, absorbing up to one-third of the India-Asia convergence through left-lateral slip (e.g., Avouac & Tapponnier, 1993; Molnar et al., 1987). The fault has been active since the late Paleocene-Eocene (L. Wu et al., 2019), currently characterized by an eastward decrease in left-slip rate, varying from ∼8 to 9 mm/year along the central segment to ∼4–5 mm/year near 95°E in the eastern segment (Zheng et al., 2017).

Various multidisciplinary geophysical cross sections have been published around the margins of the Tarim Basin, which elucidate the interactions between the Tarim lithosphere and the surrounding orogens (Figure S1 in Supporting Information S1). Compiled geophysical profiles across the Tarim Basin margins show the approximate boundaries of the Tarim lithosphere, as show in Figures 1a and 1b.

3. Data and Method

Here we synthesized multidisciplinary geophysical datasets including 2-D seismic-reflection profiles, aeromagnetic data, and satellite-based gravity data, which constrain and illuminate the crustal structure and deformation. The seismic sections constrain upper-crustal deformation. Three high-quality industry seismic reflection profiles were obtained across the Tarim Basin (Figure 1b), acquired via 2D multiple-coverage surveys by the PetroChina

Figure 1. (a) Tectonic geologic framework of the Tarim Basin and the surrounding ranges in Central Asia (Laborde et al., 2019; Yin & Nie, 1996). Much of interior and peripheral Tarim is covered by Phanerozoic strata and exposed Precambrian rocks (Z. Xu et al., 2013; Zhang et al., 2013). Geophysical cross-sections are shown as blue lines, compiled from the literature (Figure S1 in Supporting Information S1). The location of the Tarim mantle-plume head (MPH) (X. Xu et al., 2021), Bachu uplift (BCU) (H. Chen et al., 2022) and Tarim large igneous province (LIP) (S. Yang et al., 2013) are marked by thick pink curve, yellow block and dotted gray curve, respectively. Domains A and B are the regions for projecting GPS velocities along section XX'. (b) Cenozoic deformation across the Tarim Basin and its surrounding ranges. Cenozoic faults and folds are modified from Laborde et al. (2019). The thrust-dominated domains along the Western Kunlun (WKL) and Southwestern Tian Shan ranges are labeled from T1 to T3, whereas the strike-slip-dominated domains along the Altyn Tagh (ALT) and Southeastern Tian Shan ranges are labeled by S1 and S2. Three regional industry seismic-reflection profiles AA', BB' and CC' are indicated by blue lines. The boundaries of the Tarim upper-mantle lithosphere are shown with green-blue arrows numbered from A to F, which were derived from the compiled and intepreted geophysical cross sections across the Tarim Basin margins (Figure S1 in Supporting Information S1). (c) North-directed GPS velocity component along section XX' across the Tarim Basin overlain on an elevation profile. GPS stations across the domains A and B (corresponding to South of and North of 39°N, respectively) (a) and (b) are indicated by blue and pink rhombuses, respectively.

and used here with permission. The 602-km-long seismic line AA' extends northeast from the southwestern Tarim Basin to the northeast Tarim Basin, traversing through the Bachu uplift (BCU) of central Tarim. Profile line BB' is 570-km long and traverses eastward across the Tarim Basin, extending from the northwest Tarim Basin to the southeast Tarim Basin (Figure 1b). The 724-km-long profile CC' is orthogonal to, and intersects, profile BB', traversing from the southeast Tarim Basin to the northeast (Figure 1b). These three new profiles traverse the important structural domains of the Tarim Basin, including the contractional thrust belts in the west, the strike-slip fault domains in the east, the relatively undeformed interior of the Tarim Basin, and the anomalous BCU in center. Measured and previously-published borehole data were compiled to mark the stratigraphic age and sequences (e.g., Laborde et al., 2019). We follow a standard procedure to interpret the three seismic sections. The interpreted seismic horizons were checked to be consistent with proprietary industry seismic grids.

Aeromagnetic and gravity potential-field data were incorporated to image crustal compositions and the associated rheological structure (e.g., Saltus et al., 2006). The high-resolution total-field aeromagnetic anomaly intensity data used in this study originated from the aeromagnetic data set with 1 × 1 km grid and 1-km altitude (X. Xu et al., 2021, 2023), released by the China Aero Geophysics and Remote Sensing Center for Natural Resources, an affiliate of the China Geological Survey, covering the Tarim craton and its surrounding Tian Shan and Tibetan plateau. The Earth Magnetic Anomaly Grid V2 data set (Maus et al., 2009) is used to fill the aeromagnetic data gaps. We use the Oasis Montaj software (Geosoft, 2021) to merge the two magnetic grids by the suture-stitch method and to further correct the merged gird by the reduction to pole approach (Figure 2a). Finally, we use a three-dimensional (3-D) regularized magnetic inversion (Hu et al., 2019) to investigate crustal-scale structure of magnetization intensity for the area of 75°E–90°E and 34°N–40°N (X. Xu et al., 2023) (Figure 3).

Residual gravity anomalies are an effective potential-field signal for mapping the lateral density variations in the crust, especially for tectonic sedimentary basins where the basement is buried by thick sediments (e.g., Skeels, 1967). We extracted the original gravity data from the high-resolution satellite-derived free-air gravity grid (Figure S3a in Supporting Information S1) (Sandwell et al., 2014), and subtracted the gravity value of 50-km upward continuation to generate the residual gravity data used here (Figure 2b and Figure S3 in Supporting Information S1). As a related proxy to the gravity maps, we compiled the new Cenozoic sedimentary thickness data for the entire Tarim Basin from PetroChina. The lower horizon of Cenozoic strata was systematically picked along a high-resolution grid of industry seismic profiles covering the entire Tarim basin (Figure 2c).

4. Results

Seismic reflection profile AA' reveals that the basement and sedimentary cover in the southwestern Tarim Basin dips gently southwest. The Cenozoic foreland basin deposits thicken up to ∼10 km toward the Western Kunlun Range in the south, which forms a wedge-shaped foreland basin geometry (Figure 4a). At the northern margin of Western Kunlun Range, there are a series of discrete south-dipping fault truncations within Paleo-Mesozoic strata that represent north-directed thrust faults structure (Figure 4a). These faults are buried by syn-kinematic Cenozoic sediments. In the western Tarim Basin, the BCU domain is composed of the Precambrian crystallization basement and Proterozoic to Mesozoic sedimentary strata bounded by two conjugate thrust fault systems rooted in a deep basement-involved fault zone, forming a ∼250 × ∼150-km NW-striking basement-cored pop-up (Figure 4a). The fault truncations cut Precambrian to Cenozoic strata, thus indicating at least some Cenozoic motion on these faults. In the northwest Tarim Basin, the Cenozoic basin strata thicken to the northwest, forming a wedge-shaped foreland basin geometry that is up to 7 km thick (Figure 5). At the southern margin of the northwestern Tian Shan range, a series of northwest-dipping thrust truncations cut pre-Cenozoic rocks as part of a southeast-directed thrust system that encroaches on northwest Tarim Basin (e.g., the Kepingtage thrust zone).

In the eastern Tarim Basin, along the margin of the Altyn Tagh range, there is less compelling evidence for a complex fold-thrust system, but rather there are subvertical reflector truncations that cut mostly pre-Cenozoic strata (Figure 4b). In seismic profile BB', Carboniferous strata are sharply truncated by steep faults (Figure 4b). Their geometry suggests these truncations are strike-slip or oblique thrust-strike-slip features, and profile BB' crosses the left-slip Cherchen fault trace (Figure 1b). Cenozoic deposits near this fault are gently folded, but there is no profile-scale wedge-shaped geometry indicative of a flexural basin deposit. Cenozoic deposits are cut by the Cherchen fault (Figure 4b). Profile CC' also shows gently folded to flat Cenozoic reflectors in the eastern Tarim Basin. Pre-Cenozoic strata are warped at depth, which is interpreted to result from east-dipping thrust or oblique-thrust faults emanating from the Altyn Tagh Range (Figure 5). The northeast Tarim Basin exhibits some

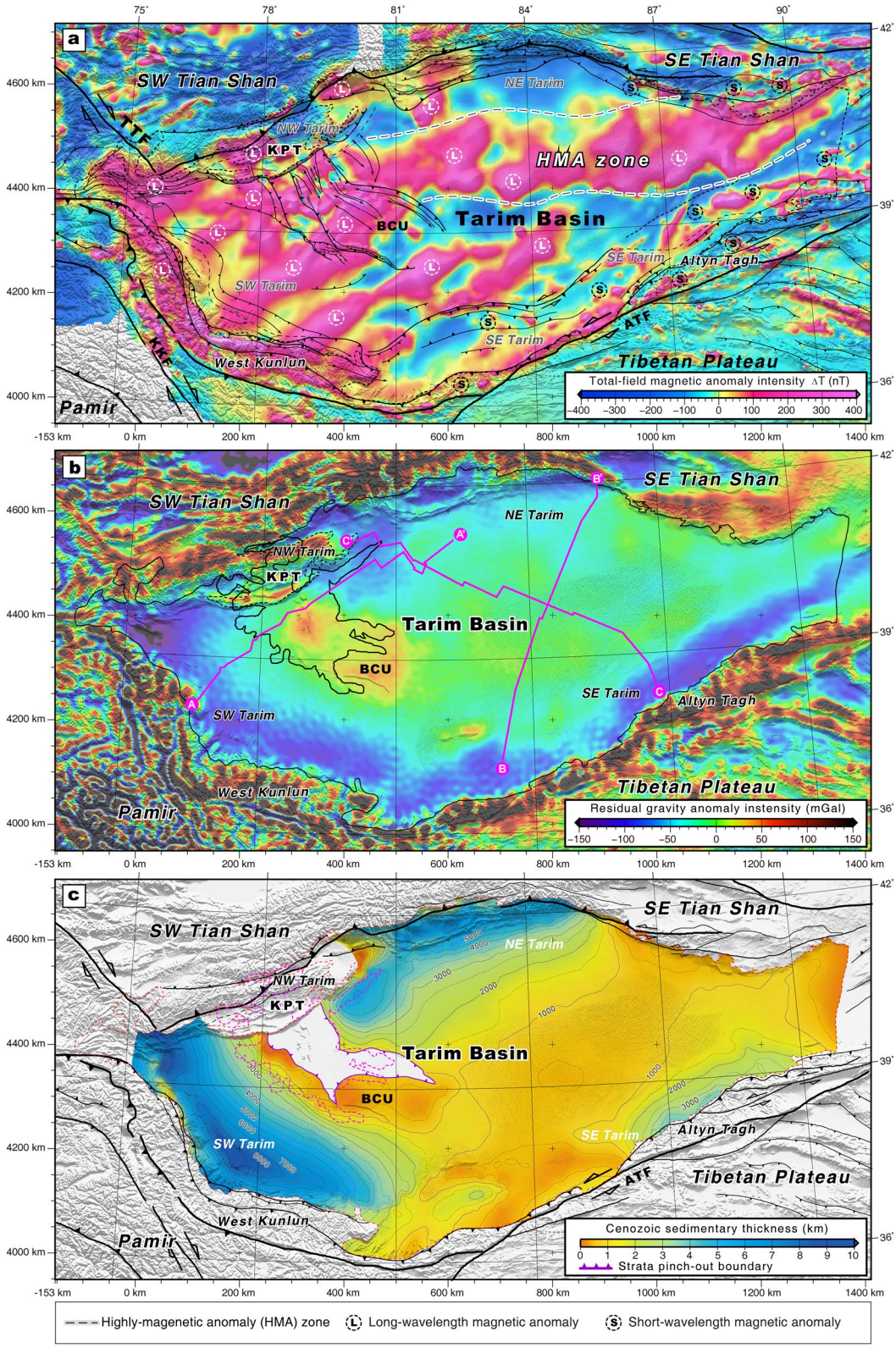

Figure 2.

subvertical faults that cut mostly pre-Cenozoic deposits (Figure 5). There is no evidence for a major thrust system or flexural subsidence in this part of the northeast Tarim Basin and southeastern Tian Shan (Figures 1, 2b, and 5).

The gravity map shows relatively low smooth negative values in the Tarim Basin (<−50 mGal) but prominent coupled gravity highs and lows, corresponding to maximum (>150 mGal) and minimum (<−150 mGal) values in the ranges around the basin (Figure 2b). Some of the most negative basin values (∼<−150 mGal) are observed within the Tarim Basin near the Western Kunlun and southwestern Tian Shan ranges. The piedmonts of the western portion of southwestern Tian Shan and southeastern Tian Shan are marked by subtle and obvious gravity highs of ∼>20 and ∼50 mGal, respectively (Figure 2b). There are subtle gravity highs that characterize the central Tarim Basin (0–20 mGal), especially the domain of the BCU that is expressed by a substantial gravity high (∼>50 mGal) (Figure 2b).

The Cenozoic sedimentary thickness map shows similar patterns to the residual gravity anomaly map (Figures 2b and 2c). The maximum sediment thicknesses of >∼10 km is distributed across the front zones of Western Kunlun and southwestern Tian Shan ranges, except the Kepingtage fold-thrust belt that has minimal Cenozoic subsidence (Figure 2c). Cenozoic sediment thicknesses of <∼1 km are observed across the BCU and the piedmonts of the Altyn Tagh and southeastern Tian Shan ranges. Sediments thicken adjacent to the Altyn Tagh Range to ∼3.5 km (Figure 2c).

The aeromagnetic map shows that most of the Tarim Basin is comprised of long-wavelength positive magnetic anomalies, especially the highly (high-amplitude) magnetic anomaly (HMA) zone located in the central portion of eastern Tarim (Figure 2a). Notable exceptions with negative or minor short-wavelength magnetic anomalies include the northeastern and southeastern Tarim Basin and the adjacent mountain ranges (Figure 2a). A 3D regularized magnetic inversion reveals that the lower crust across most of the Tarim Basin is dominated by series of highly magnetic anomalies (values >than 1.8 A/m) except for the northeastern and southeastern Tarim Basin that shows extremely low magnetization intensity (values of <1 A/m) (Figures 3 and 6). In contrast, the upper crust of the Tarim Basin is mostly characterized by lower magnetization (<0.5 A/m), except the northwestern Tarim domain that yields very high magnetic intensity (>1.8 A/m) (Figure 7).

5. Discussion

5.1. Distinct Modes of Intra-Continental Deformation Across the Tarim Basin

There is a notable dichotomy between thrust-dominated deformation within and around the western Tarim domain and strike-slip-dominated deformation in the eastern Tarim domain (Figure 1b). Cenozoic contractional deformation around the Tarim Basin is mainly concentrated at the frontal domain of Western Kunlun and northwestern Tian Shan ranges, whereas strike-slip-related deformation is accommodated along the Altyn Tagh and southwestern Tian Shan ranges (Figures 1, 4, and 5). These patterns influence Cenozoic sedimentation as observed through sediment thickness and residual gravity maps (Figures 2b and 2c). Thrust-induced loading of the Tarim Basin leads to thick Cenozoic deposits in the west, thickening toward the margin of the Tarim Basin as they are bounded by basin-verging thrust belts. Conversely, the eastern Tarim Basin does not display thick Cenozoic sediments, which is more consistent with strike-slip deformation without significant thrust-induced loading. Just north of the Altyn Tagh Range is minor subsidence and related sedimentation observed in the gravity and sediment maps (∼3 km) that reflects loading of the Tarim Basin caused by the transpressional deformation observed within this bend in the ATF (e.g., Cowgill et al., 2004; Gao et al., 2022). These observations suggest that the ranges around the western Tarim Basin have experienced more shortening and foreland-loading throughout the Cenozoic, and thus the present-day strain patterns have persisted throughout the Cenozoic.

Figure 2. (a) Composite aeromagnetic map of Tarim Basin and its surrounding orogenic ranges, depicting total-field aeromagnetic anomaly corrected by reduction to the pole (RTP), overlaid by Cenozoic faults (Laborde et al., 2019; Yin & Nie, 1996). The non-colored domains are grid gaps. Black thin lines outline the Cenozoic crustal-scale faults, and black thick lines indicate the lithospheric-scale regional faults. White circled-L and black circled-S express the long-wavelength and short wavelength magnetic anomalies, respectively. The white-black lines outline the domain of highly-magnetic anomaly (HMZ) zone. The RTP-corrected aeromagnetic anomaly maps are overlain on the shaded Etopo1 model (https://www.ngdc.noaa.gov/mgg/global/global.html). ATF, Altyn-Tagh fault; TFF, Talas-Fergana fault; KKF, Karakorum fault. (b) Residual gravity anomaly map of Tarim Basin and the surrounding ranges. Three seismic-reflection sections (AA', BB', and CC') are labeled by pink lines. Tarm Basin is characterized by low gravity values with minimum values distributed across the southwest, southeast and northeast Tarim, except the Bachu uplift and northwest Tarim (Kepingtage belt) marked by predominant gravity highs, while the surrounding orogenic belts including Pamir, Tian Shan and NE Tibetan plateau are all expressed by series of coupled gravity highs and lows. (c) Cenozoic sediment thickness map in the Tarim Basin. The interval of thickness contours is 0.5 km. The 1-km interval thickness values are overlapped, as well as the key faults around the basin. KPT, Kepingtage thrust zone; ATF, Altyn-Tagh fault; TFF, Talas-Fergana fault; KKF, Karakorum fault.

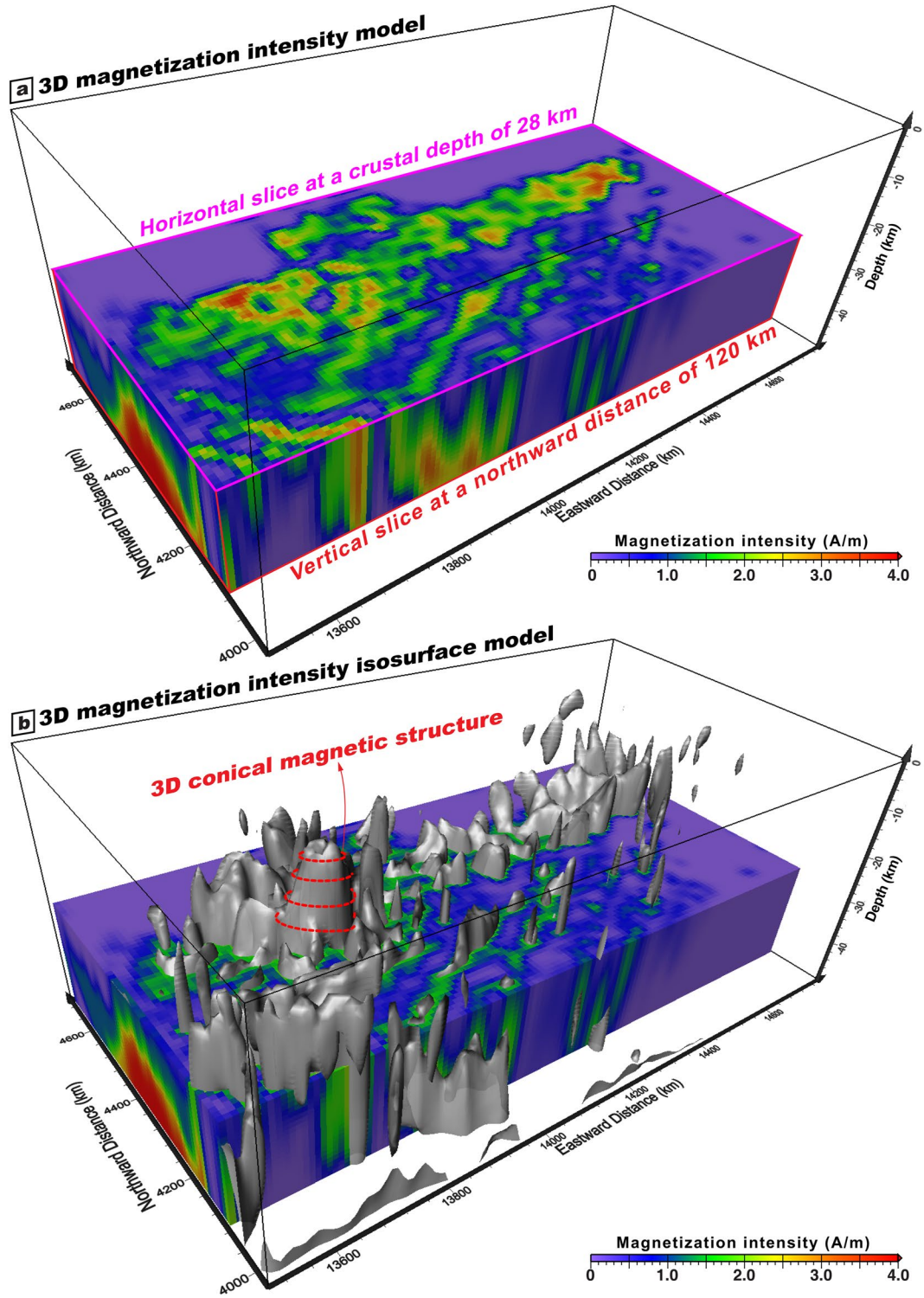

Figure 3. (a) Three-dimensional (3D) magnetization intensity model for Tarim Basin and its surrounding regions, based on the regularization inversion with 130 × 74 × 50 grid cells and 10 × 10 × 1 km resolution (X. Xu et al., 2023). 3D horizontal slice model at crustal depth of 28-km is presented here, as well as the vertical slice at northward distance of 120 km. (b) 3D visualization of iso-surface magnetization model (magnetization intensity is 1.6 A/m). The 3D comical magnetic structure is labeled by red dotted circles.

10.1029/2023TC007748

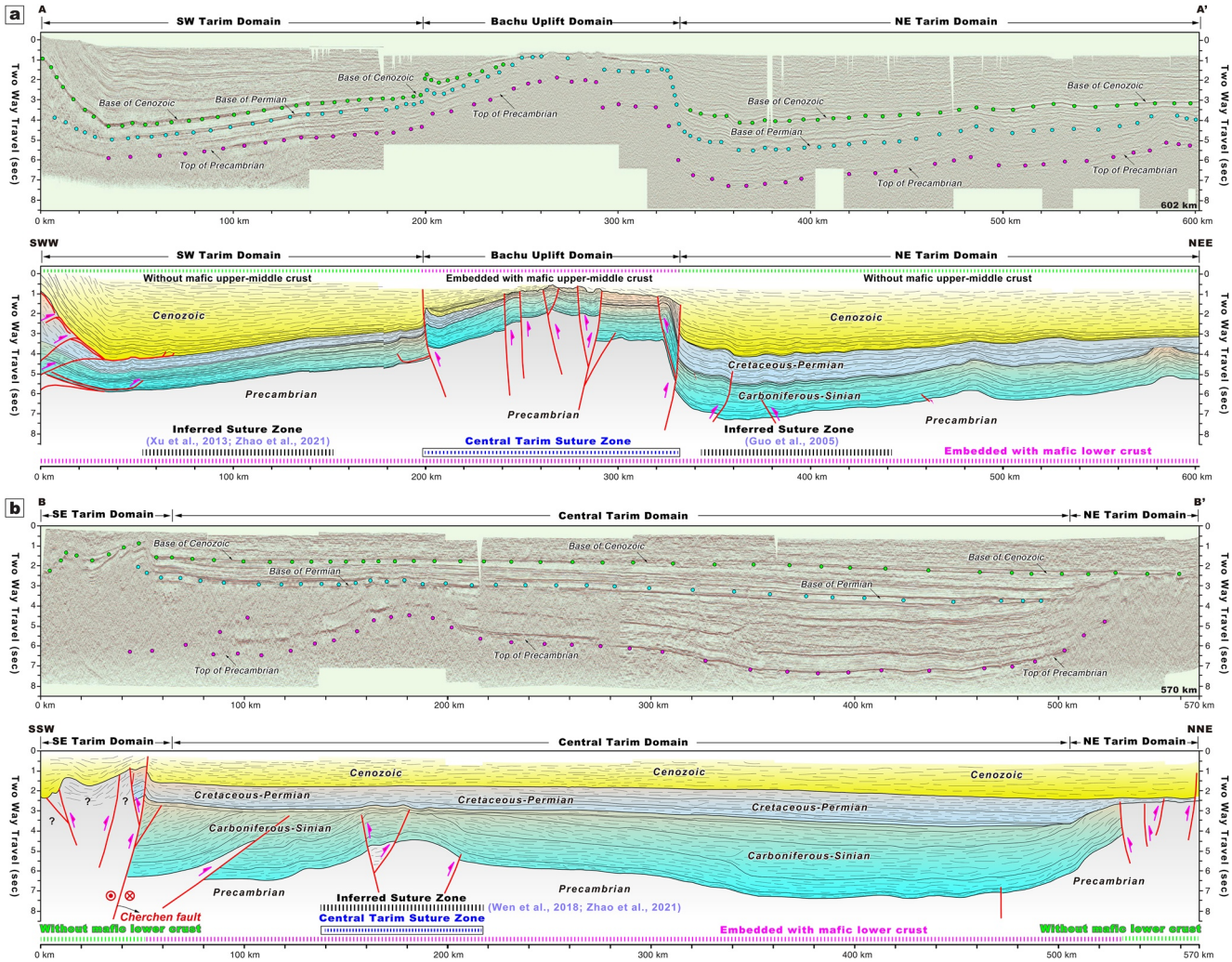

Figure 4. Uninterpreted and interpreted seismic sections AA' (a) and BB' (b) across the central-western Tarim Basin (Blue lines in Figure 1b). The black dotted line indicates the location of Central Tarim suture zone between North and South Tarim, inferred by various models (Guo et al., 2005; Wen et al., 2018; Z. Xu et al., 2013; P. Zhao et al., 2021). The blue dotted lines mark the location of inferred and predicted suture zones by various studies. The green and pink dotted lines emphasize regions that are interpreted to be embedded, or not, with a relatively mafic lower crust, respectively.

A similar, consistent deformation pattern persists for the structures observed within the basin, as imaged in this study via the seismic reflection profiles (Figure 4). The BCU experienced Cenozoic thrust-related shortening in the western Tarim Basin (Figure 1b). Conversely, the left-slip Cherchen fault in southeastern Tarim Basin parallels the ATF with similar kinematics (Tian et al., 2023) (Figure 1a), and more minor northeast-striking left-slip faults have been observed via 3D seismic grid with small displacements between the Cherchen fault and the eastern extent of the BCU (Qiu et al., 2022).

Estimates of N-S-oriented crustal shortening decrease eastward from western Tarim (~80 km minimum shortening) to eastern Tarim (~35 km minimum shortening) (Laborde et al., 2019) (Figure 1b), consistent with the eastward-decreasing trend of north-directed convergence in the GPS data (Figure 1c). The western Tarim region notably accommodates >10 mm/year of north-south convergence, whereas the eastern Tarim region accommodates only several mm/year of north-south convergence (Figure 1c). The east-directed component of the GPS velocity field increases from the western Tarim to eastern Tarim (Figure S2 in Supporting Information S1), consistent with more lateral motion of the crust. In summary available structural and geophysical data demonstrate that the western Tarim Basin and surrounding ranges experienced predominately contractional thrust-related deformation, whereas the eastern Tarim Basin accommodated more discrete strike-slip deformation.

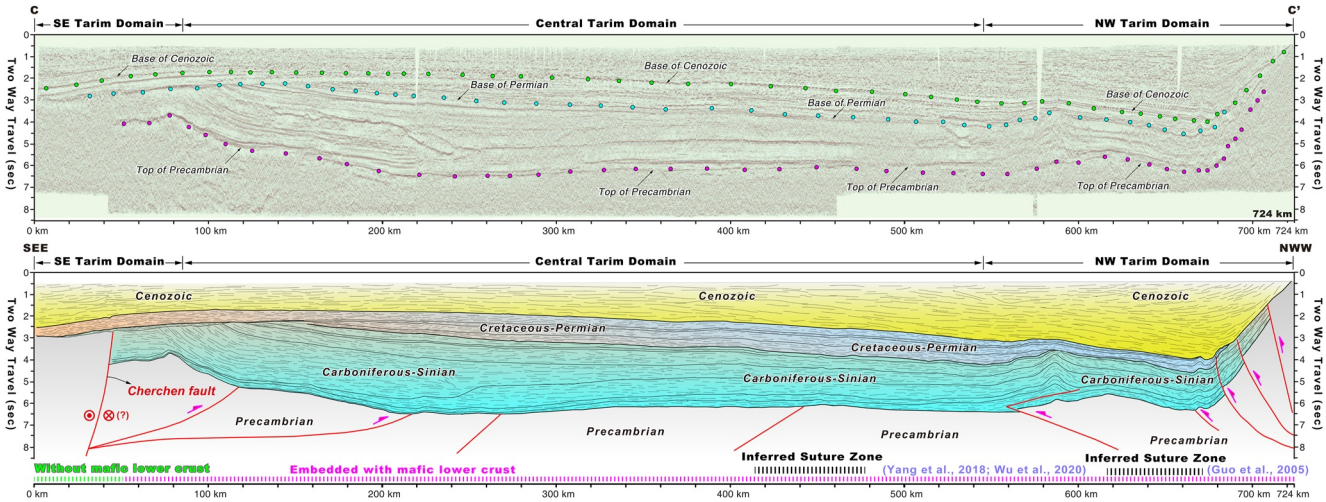

Figure 5. Uninterpreted and interpreted seismic sections CC' across the central-eastern Tarim craton (Blue line in Figure 1b). These colored dotted lines are same to that of Figure 4. The location of Central Tarim suture zone between North and South Tarim are inferred by several different publications (Guo et al., 2005; G. Wu et al., 2020; H. Yang et al., 2018).

5.2. Structure and Compositional Patterns Across the Tarim Basin

The aeromagnetic maps and our 3D crustal-scale inversion of magnetization intensity for the Tarim Basin and the surrounding ranges reveal distinct features in the lower crust. Most of the Tarim Basin exhibits high-amplitude magnetic anomalies, except the southeastern and northeastern parts of the basin (Figure 6). Bulk crust-scale magnetization is primarily dependent on the total content of mafic rock in the crust (Grant, 1985; Saltus

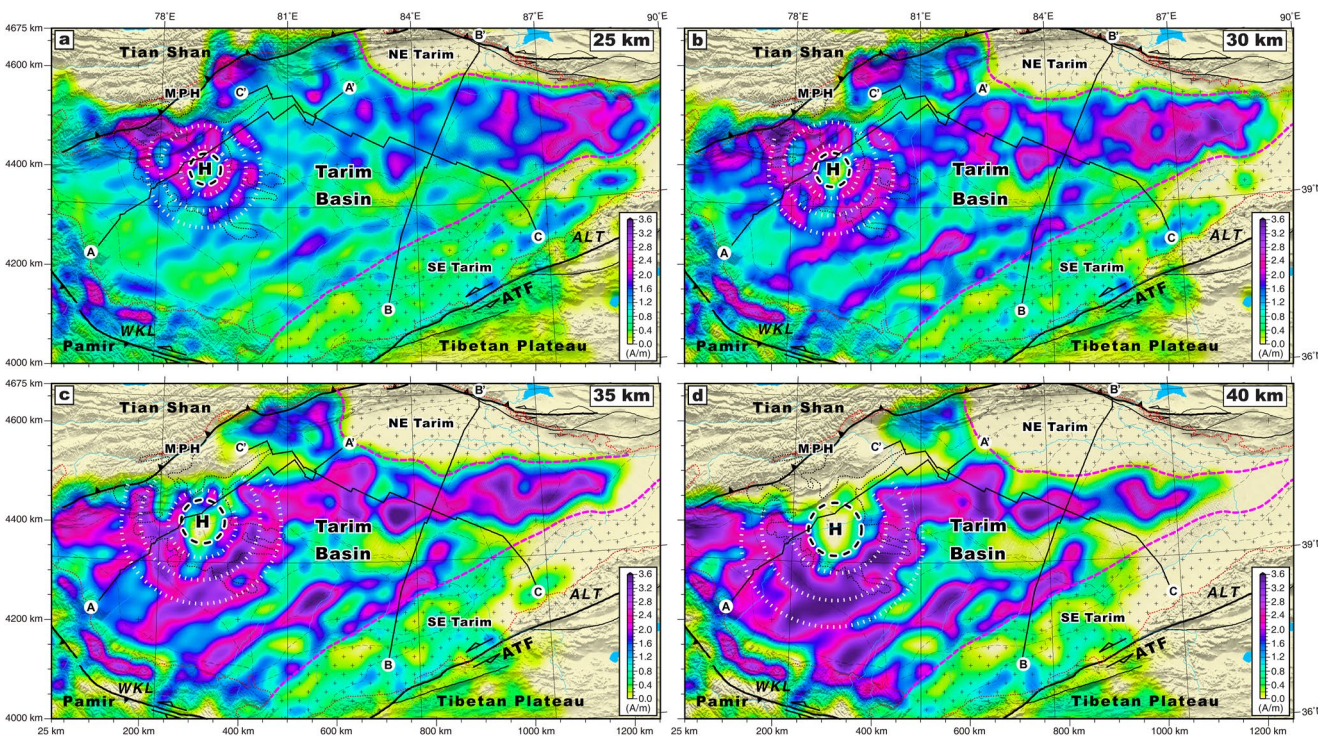

Figure 6. Horizontal slices of magnetization intensity at the middle-lower crust of Tarim Basin and its surrounding ranges at depths of 25 km (a), 30 km (b), 35 km (c) and 40 km (d). The pink dotted curve outlines the boundary between mafic and non-mafic mid-lower crust. Symbols of plus (+) mark the distribution of felsic mid-lower crust. Dotted-circled H indicates the inferred Tarim plume head. White arrows and dotted circular show interpreted radial patterns of mid-lower crust mafic intrusion related to the Permian plume. Three regional seismic-reflection sections are overlaid.

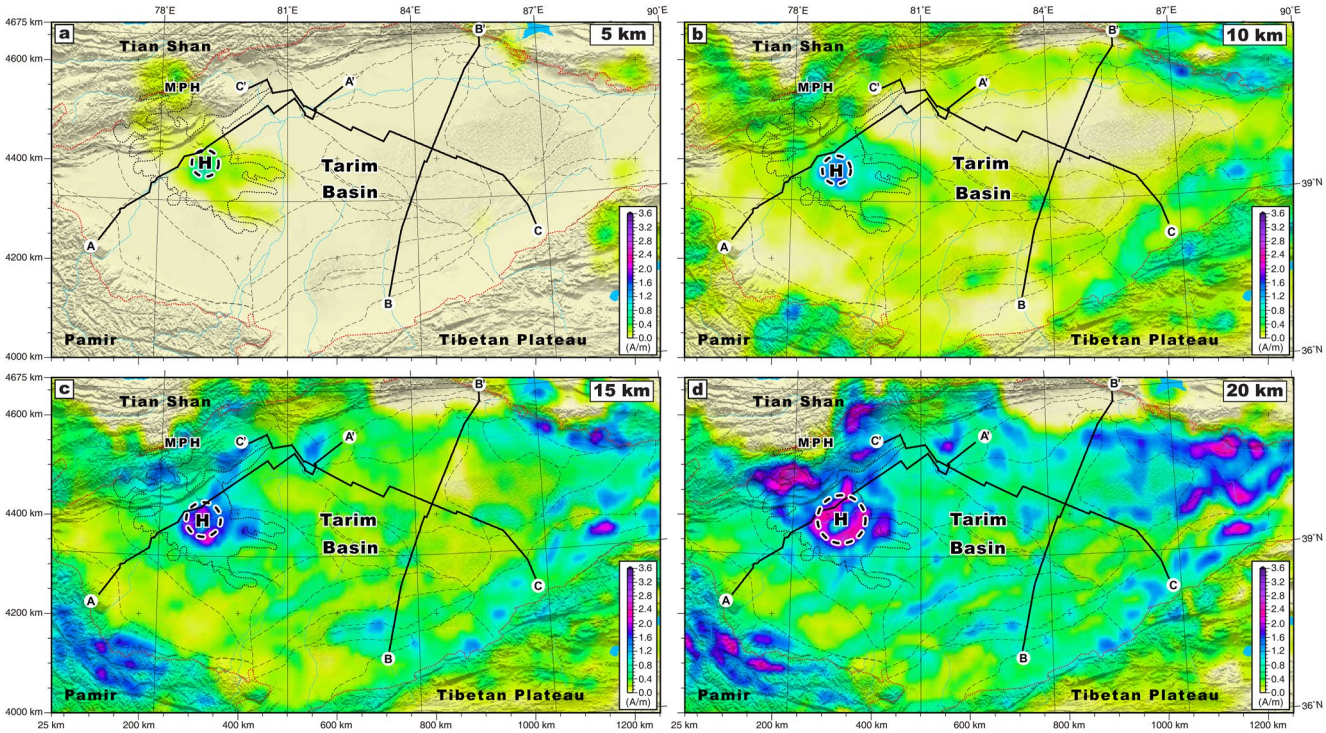

Figure 7. Horizontal slices of magnetization intensity at the upper-middle crust of Tarim Basin and its surrounding ranges at depth of 5 km (a), 10 km (b), 15 km (c) and 20 km (d). Dotted-circled H indicates the inferred Tarim plume head (X. Xu et al., 2023). Three regional seismic-reflection sections of AA', BB' and CC' are overlaid.

et al., 1999), such that crust dominated by mafic rock is more magnetized than crust that is more felsic. This inference is supported by the magnetic susceptibility of various rocks measured across the entire continental China ($n = 248{,}756$ samples) (Xiong et al., 2016). The P-wave velocity structure of the Tarim crust (J. Zhao et al., 2006) confirms that regions of the lower crust with higher magnetic intensity in our datasets are more seismically fast, and thus interpreted as more mafic in composition. Therefore, we interpret that series of high-amplitude, long-wavelength positive magnetic anomalies distributed across much of the Tarim Basin originate from a relatively mafic lower crust. Conversely, the high-amplitude, short-wavelength magnetic patches in the southeast and northeastern Tarim basin do not correspond to a lower crust enriched in mafic materials. Based on the spatial correspondence of long-wavelength magnetic signals inferred to represent a mafic lower crust and the location of the impinged Permian mantle plume in western Tarim Basin (Figures 2a and 6), we infer that much of the dense (Deng et al., 2017) mafic lower crust in the Tarim Basin was generated due to plume-related intrusions and underplating (X. Xu et al., 2021, 2023). Furthermore, our high-resolution 3D inverted magnetic intensity model shows a crustal-scale conical structure that penetrates to ~50-km-depth (Figures 3, 7, and 9) beneath the radial magnetic lineaments in the western Tarim Basin that correspond plume-modified crust (X. Xu et al., 2021, 2023). Our inversion does not artificially introduce any structure in advance, so this conical feature directly reflects the distribution of magnetic bodies (X. Xu et al., 2023). We interpret that the regions of southeast and northeast Tarim Basin that do not exhibit such magnetic anomalies were thus less impacted by the Permian plume event.

There is a major linear west-trending high-amplitude magnetic strip across the Tarim Basin (Figure 8a) that has been previously interpreted as a Proterozoic suture zone or arc between North and South Tarim referred to as the Central Tarim suture zone (Figure 8a) (e.g., Guo et al., 2005; G. Wu et al., 2020; H. Yang et al., 2018). The age of this suture zone is interpreted to be either Late Paleoproterozoic or Neoproterozoic based on sparse geochemical and geochronologic data collected along this magnetic strip, mostly from dill core (e.g., Guo et al., 2005; G. Wu et al., 2020; H. Yang et al., 2018; P. Zhao et al., 2021; Zuza & Yin, 2017). However, our 3D magnetic inversion shows that this long-wavelength, high-amplitude aeromagnetic anomaly is most likely derived from lower crustal mafic bodies instead of discrete transcrustal paleo-subduction interfaces (Figures 3 and 6). The seismic reflection profiles that image to ~15 km depth (Figures 4 and 5) do not uniquely resolve any suture zone (Figures 8c–8e) (e.g., Guo et al., 2005; Wen et al., 2018; H. Yang et al., 2018; P. Zhao et al., 2021).

10.1029/2023TC007748

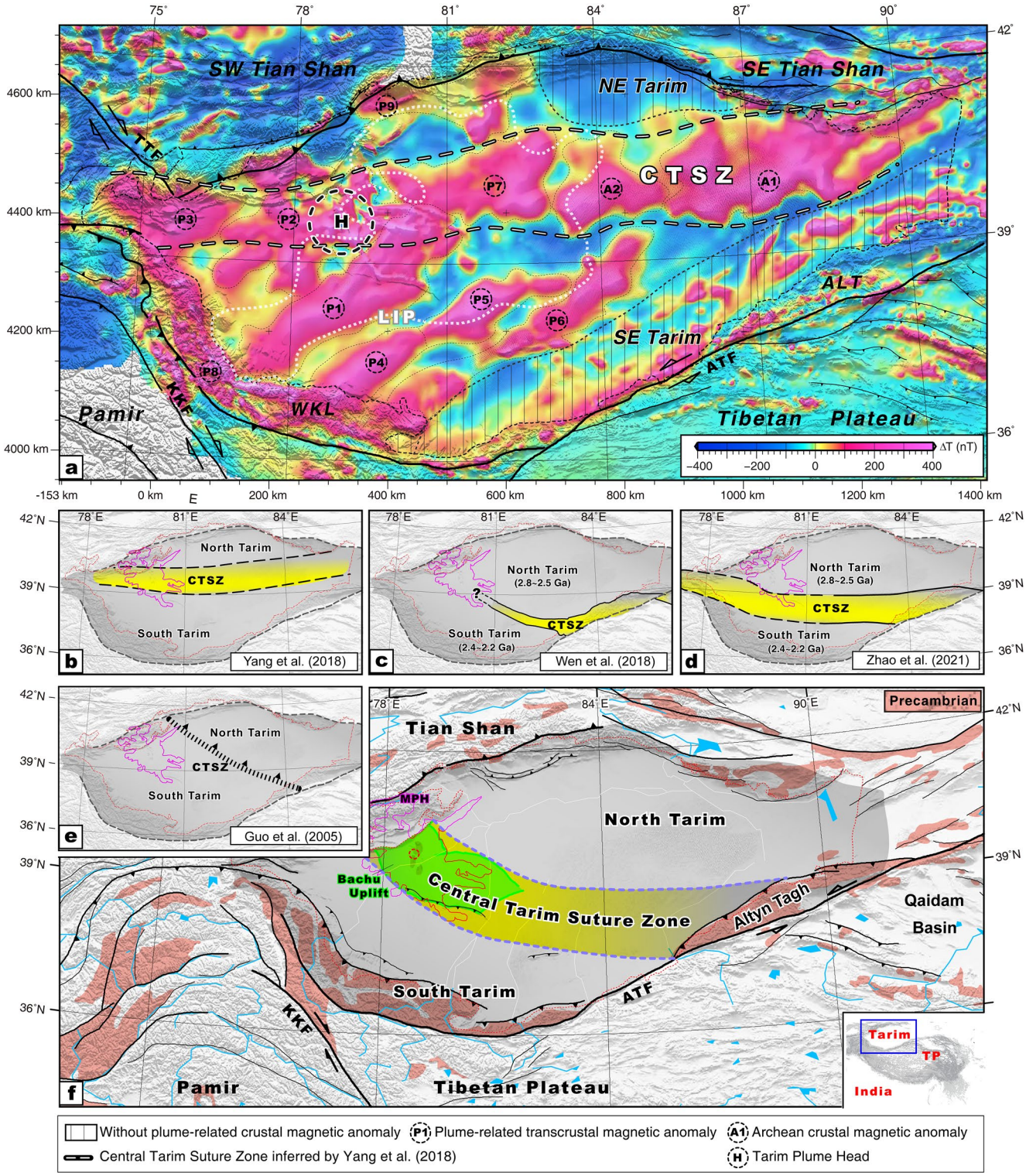

Figure 8. Interpretation and origin of high-amplitude, long-wavelength aeromagnetic anomalies (a) across the Tarim Basin and potential locations of Central Tarim suture zone (b)–(f). Locations of Central Tarim suture zone proposed by presentative models (b)–(e) (e.g., Guo et al., 2005; Wen et al., 2018; G. Wu et al., 2020; H. Yang et al., 2018; P. Zhao et al., 2021) and our interpreted model of f (f).

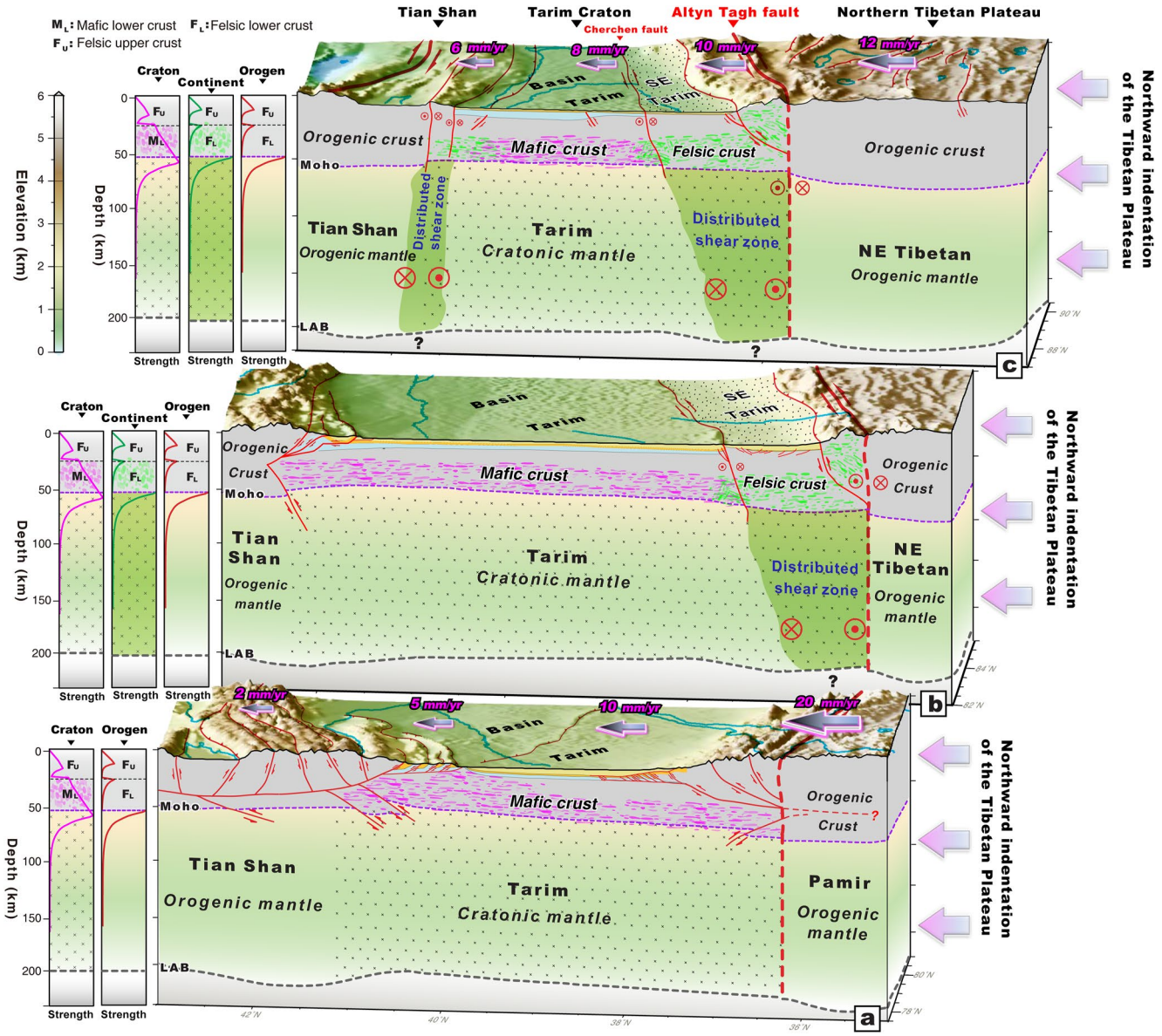

Figure 9. Schematic three-dimensional lithospheric-scale section across western (a), central (b) and eastern (c) Tarim Basin and their surrounding ranges, illustrating the proposed deformation processes active within and around the Tarim Basin (locations labeled in Figure 1b). Crustal strength profiles of an orogen, continent, and craton show inferred rheological structure differences of the lower continental crust caused by a more felsic versus more mafic. The felsic and mafic lower crust are represented by plagioclase An75 and dry diabase, respectively (L. Chen et al., 2017). The upper crust and lithosphere mantle are represented by wet quartzite and dry olivine, respectively. The strength of the whole lithosphere is defined by the depth-integral of stress profile (L. Chen et al., 2017). The more rigid lower crust in the western Tarim acts like a rigid underplating block that may be more strongly coupled with the underlying mantle, forming a crustal wedge inserted into the crust of weaker ranges (Tian et al., 2021) (a) and (b). The three-dimensional pink arrows represent the northward GPS velocities, of which the sizes are proportional to these corresponding velocity values labeled above. Yellow, light yellow and pool blue blocks correspond to Cenozoic, Mesozoic and Paleozoic sediments, respectively. Pink and green speckles mark the mafic and felsic crustal rocks, respectively. Blue-colored rivers are overlain on the topographic model. LAB, lithosphere-asthenosphere boundary.

Therefore, we argue that the major west-trending magnetic anomaly does not represent the Central Tarim suture zone but may represent an Archean nucleus, similar to these high-amplitude aeromagnetic anomaly zones distributed across the Ordos and Sichuan cratons and other cratons globally, such as the Indian, Australian, and African cratons (X. Xu et al., 2023). However, our interpreted seismic profiles did observe two regions of focused deformation that may reflect deep reactivation of a suture zone across the Tarim Basin, including the BCU and a smaller uplift in the central Tarim Basin (Figure 4). We speculate that a deep suture zone could have stretched from the Altyn Tagh Range through these uplifts to the northwest (Figure 8f), which is parallel to an

interpreted suture zone that would have stretched southeast from the Altyn Tagh Range across northern Tibet (Guo et al., 2005; Zuza & Yin, 2017).

5.3. Lower Crust Rheology Controls Intra-Crustal Detachments and the Mode of Intra-Continental Orogeny

The different deformation styles around the Tarim Basin, from thrusting in the west to strike-slip faulting in the east, indicate variable modes of strain accommodation and localization during Cenozoic Himalayan-Tibetan orogeny around the Tarim Basin (Figure 1). Deciphering the first-order controls for these different deformation modes is thus critical for understanding strain partitioning in an intra-plate setting. Several potential drivers are proposed to cause the differential deformation between the western and eastern Tarim Basin, including differences in crustal thickness, pre-Cenozoic geologic histories, boundary conditions or variable crustal strengths (e.g., L. Chen et al., 2017; Molnar et al., 1993; Schellart et al., 2019; Tapponnier et al., 1982; J. Yang et al., 2020; Yin, 2010). It is notable that thicker crust with higher surface elevations favors strike-slip or normal-fault regimes (e.g., Molnar et al., 1993), but there are no present-day crustal thickness variations between the western and eastern Tarim Basins (Figure S4 in Supporting Information S1) (e.g., Bao et al., 2015). The Proterozoic-Paleozoic histories of Tarim and Tibet are generally similar, including a west-trending Neoproterozoic suture zone that divides the north and south Tarim continents (Guo et al., 2005; P. Zhao et al., 2021) and early Paleozoic orogeny that impacted the integrated Tarim and Tibetan crust (C. Wu et al., 2016; Xiao et al., 2003; Zuza et al., 2018). Given that there were no remarkable differences regarding the pre-Mesozoic geology around the Tarim Basin, one of two alternative mechanisms is envisioned to control the spatiotemporal mode of crust-scale deformation surrounding the basin: (a) varying boundary conditions or (b) variable low-crust strength caused by the impingement of the Tarim Permian mantle plume.

It has long been argued that variable boundary conditions surrounding central Asia may impact the styles of intraplate deformation (e.g., Schellart et al., 2019; Tapponnier et al., 1982; Yin, 2010), with the indenting boundary of the Indian plate in the south, the relatively free boundary of West Pacific plate to the east, and the more fixed lateral boundaries of central Asia to the west and north. These boundary conditions may favor an overall flow of the crust toward the lateral free boundary of the Pacific-Asian margin, leading to more lateral translation, block rotation, and strike-slip faulting in the east than the west. Although there have been decades of extrusion-type tectonic models (e.g., Avouac & Tapponnier, 1993; Tapponnier et al., 1982), updated knowledge of the strike-slip faulting in central and northern Tibetan Plateau show that the crust is not laterally translating toward the western Pacific ocean (e.g., Cheng et al., 2021; J. Yang et al., 2020; Zuza & Yin, 2016). The major strike-slip faults embedded with the plateau are not linked structures to the eastern free boundary. For example, the eastern Kunlun and Haiyuan fault tips terminate at the boundary of the plateau and accommodate rotation and/or northward strain dissipation (Cheng et al., 2021; Duvall & Clark, 2010; England & Molnar, 1990; J. Yang et al., 2020; Zuza & Yin, 2016), which is evidence against a broad flow pattern of Tibet toward the eastern lateral free boundary. Lastly, there is a major right-slip fault system to the northwest of the Tarim Basin (e.g., Cobbold & Davy, 1988; Yin, 2010), which implies that strike-slip faulting occurs toward the fixed boundary of central Asia, and thus strike-slip-dominated deformation does not uniquely reflect block translation toward a free boundary condition.

Another test of the control of boundary conditions is to examine the GPS velocity field as it relates to regional patterns of faulting around the Tarim Basin. GPS vectors in the Tibetan crust to the southwest and southeast of the Tarim Basin show similar patterns approaching the southern boundaries of the Tarim Basin (Figure 1a). That is, if the eastern free boundary condition was driving the Tibetan plateau crust to migrate to the east, the velocity field would be expected to curve toward the east without any influence from the Tarim lithosphere. Instead, vectors converge against Tarim Basin boundaries with similar vectors (magnitudes and directions) (Figure 1a), and there is no obvious broader pattern approaching Tarim Basin where the vectors flow toward the eastern free boundary. In fact, the GPS vectors to the southwest of Tarim are more parallel to the fault-boundaries of the Tarim Basin and those to the southeast of Tarim are more oblique to the boundaries of the basin. This relationship would favor strike-slip faulting in the southwest Tarim and contractional thrust faulting in the southeast Tarim Basin, which is opposite of our observations (Figure 1).

Alternatively, another significant difference between the western and eastern domains of the Tarim Basin is that the Permian mantle plume impinged in the western Tarim, and aeromagnetic data suggests that the plume

head and intruded crust were more restricted to the western Tarim Basin than the eastern Tarim Basin (X. Xu et al., 2021, 2023). One interpretation is that the mantle plume more strongly modified the crust in the western Tarim Basin, which led to thrust-dominated deformation in the west, whereas strike-slip dominated faulting occurred where this plume-modification was weaker in the eastern Tarim Basin (Figure 1b). This interpretation suggests that the Permian mantle plume and its modification of the Tarim lithosphere controls how Cenozoic strain is partitioned around the Tarim Basin, which simultaneously explains why the Tarim Basin resisted Cenozoic strain and why there are variable modes of crustal deformation around the basin.

The strength of the lower crust is strongly controlled by its composition and abundance of felsic versus mafic rocks (Figure S5 in Supporting Information S1) (e.g., Brace & Kohlstedt, 1980; Bürgmann & Dresen, 2008; L. Chen et al., 2017; Goetze & Evans, 1979). Such lower-crustal compositional variations can be effectively distinguished by our high-resolution aeromagnetic imaging and inversion (Figures 3 and 5). As discussed above, the western Tarim Basin is characterized by a highly-magnetized lower crust, which implies that it is more mafic than the eastern basin. The abundance of mafic rocks in lower crust of the western Tarim Basin implies that the lower crust should be mechanically stronger with a more viscous rheology. Conversely, the eastern Tarim Basin does not show similar enrichment of a mafic lower crust, and therefore this crust may be more homogenous with a moderate strength.

Guided by the correlation between this inferred lower crustal viscosity and the differing modes of strain partitioning, we suggest that the differing modes of intracontinental orogeny and associated crustal shortening are controlled by the rheology of the lower crust. The more rigid lower crust in the western Tarim acts like a rigid underplating block that may be more strongly coupled with the underlying mantle, forming a crustal wedge inserted into the crust of weaker ranges (Tian et al., 2021) (Figures 9a and 9b). When vertically uniform horizontal stresses from India-Asia convergence act on the Tarim lithosphere, the mechanically-weak upper crust easily becomes decoupled from the mechanically-rigid lower crust, developing a fold-and-thrust belt (Figure 9a). The rheological strength contrasts within the lithospheric column promote crustal decoupling to result in a more distributed record of upper crustal shortening on the margins of the rigid Tarim lower crust. For example, through a compilation of global orogens, Mouthereau et al. (2013) showed that a strong lower crust and coupled mantle in deforming regions inhibits the formation of deep crustal shear zones to therefore favor upper crust detachment faulting and shortening. Conversely, in the eastern Tarim Basin, the crust is not enriched in mafic materials and is thus more vertically uniform in composition and strength, which promotes a more coupled crustal column that favors lithosphere-scale strike-slip faulting (Figures 9b and 9c). Shear zones are able to cut through the lower crust more easily because it was not strengthened by mafic intrusions. Thus, vertical decoupling and the establishment of detachment faults drives distributed intra-plate deformation, whereas more coupled crustal columns may favor strike-slip faulting here.

Our interpretations are somewhat counterintuitive with the idea that a weak lower crust may permit crust-mantle decoupling. Specifically, if the lower crust exhibits a low viscosity, the middle-upper crust is thought to detach from the lithospheric mantle (e.g., Hopper & Roger Buck, 1998; Royden, 1996). However, our observations suggest that a strong lower crust may permit mantle-lower crustal coupling and promote decoupling of the upper crust to deform as a detached thrust wedge. This mechanism permits rigid indentation of a strong mid-lower crust into bounding intra-plate orogens that experience upper-crustal shortening. In the case of more homogenous crustal column, deformation would be expected to be more distributed (Calignano et al., 2015), propagating into the Tarim Basin. This is not observed, except in the eastern Tarim Basin, where subvertical strike-slip faults are observed cutting the entire crust, which suggests a relatively homogenously strong crustal column that is entirely cut by faulting.

The origin of the Cenozoic basement-cored BCU within the west-central Tarim Basin has long been debated (e.g., H. Chen et al., 2022; Laborde et al., 2019). Previous geophysical observations of the uplift had limited lateral resolutions of >200 km, which hindered evaluation of this structure. Our high-resolution crustal-scale magnetic inversion revealed that the 3D conical mafic structure was located directly beneath the Bachu domain (Figures 3, 7, and 9). We interpret that this feature is a relic of Permian plume magmatism based on its spatial location beneath the Permian volcanic fields and our refined magnetic imaging of the radiating dike geometry of the plume head (Figures 3, 7, and 10) (X. Xu et al., 2021, 2023). Based on its strong magnetic character and interpreted mafic composition, this feature would have been relatively strong, and therefore it may have efficiently focused stress along its boundaries to drive focused strain (e.g., Calignano et al., 2015; Campbell, 1978).

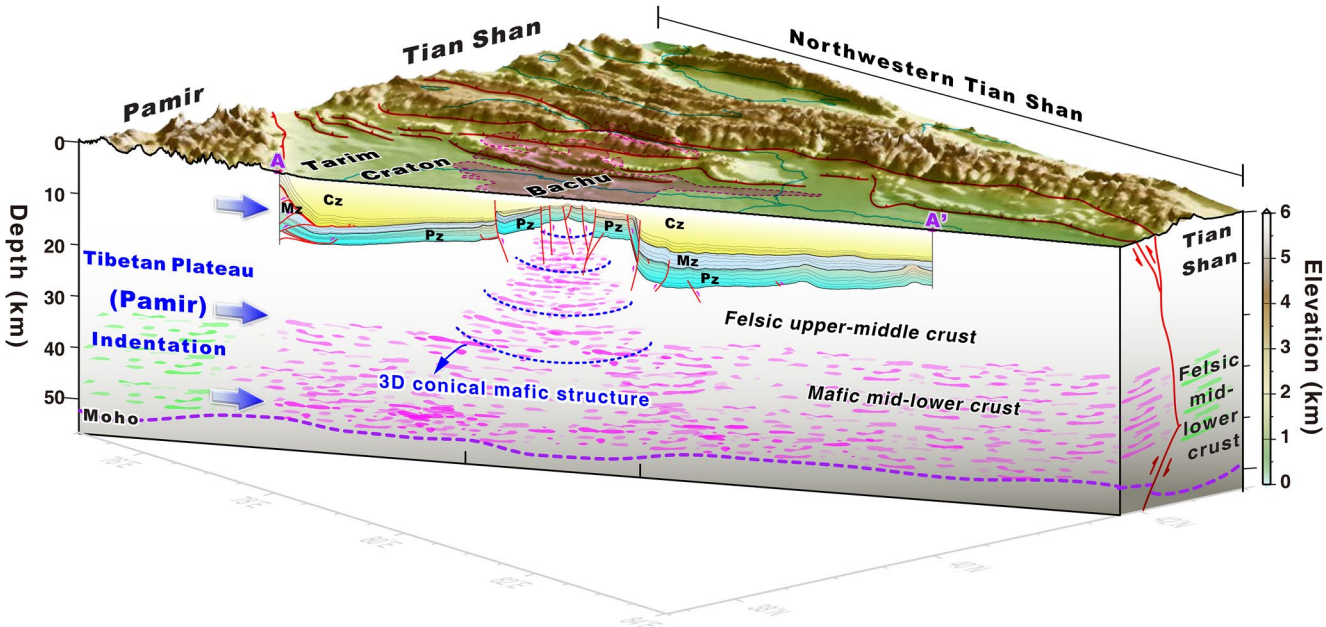

Figure 10. Upper-middle crustal-scale deformation of the Bachu uplift (BCU), western Tarim. Only the BCU is underlain by 3D conical-like mafic structure of upper-middle crust, imaged by the 3D inversion of magnetization intensity (Figure 3).

Furthermore, the BCU is parallel to the Western Kunlun fold-and-thrust belt, but nearly orthogonal to the southwestern margin of the Tian Shan (Figure 1). This geometric relationship may suggest that the BCU originated due to upper crustal displacement originating from the Western Kunlun Range, decoupled from the lower crust. Strain focused around the relatively strong and anomalous mafic conical structure to drive local deformation around the BCU that paralleled the Western Kunlun Range.

The arcuate Kepingtage fold-thrust belt of the southwestern Tian Shan is a unique domain where south-directed thin-skinned thrusting (e.g., Yin et al., 1998) encroaches within the Tarim Basin and there is minimal Cenozoic tectonic subsidence or foreland sedimentation (Yin et al., 1998) (Figure 2). The southeast, frontal thrust fault of this system intersects and truncates the BCU. Part of the unique deformational style of the Kepingtage fold-thrust belt likely originates from its interaction with the BCU (Laborde et al., 2019). Our observations broadly support this interpretation. We further speculate that the concentration of Permian plume-related intrusions under the BCU, just toward the foreland of the Kepingtage thrust belt may have simultaneously acted as a rigid barrier in the mid-lower crust and promoted decoupling of the upper crust, to develop the south-vergent thin-skinned Kepingtage thrust belt (Figures 9a and 10).

5.4. Analogous Strain Partitioning Along the Eastern Margin of the Tibetan Plateau

Herein we have proposed that lower crustal rheology controls differential strain partitioning in an intra-plate orogen. To test the generality of this hypothesis, we examined another intra-plate setting where strain is variably partitioned between thrusting and strike-slip faulting. Specifically, along the eastern margin of the Tibetan plateau, the Longmen Shan accommodates convergence between Sichuan craton and the plateau (e.g., Burchfiel et al., 1989) (Figure 11). The Longmenshan fault zone expresses contrasting behavior between its southern and central-northern segments, with thrust-dominated deformation in the south and right-slip-dominated deformation in the north (e.g., Jiang et al., 2019; Shen et al., 2009). A Cenozoic foreland basin only preserved at the range front of the southern portion with a maximum sediment thickness of 3.5 km, whereas it is peculiarly absent along the central and northern segment (Wang et al., 2006) (Figure 11). The southern fault zone accommodated crustal shortening and dip-slip thrust faulting that loaded the foreland to develop a thicker foreland basin, whereas the significantly reduced loading to the northeast did not develop an associated foreland subsidence.

One of the most striking along-strike differences of the Longmen Shan foreland geology is that the Permian Emeishan plume and coupled large igneous province were emplaced in the south, with extensive flood basalts

10.1029/2023TC007748

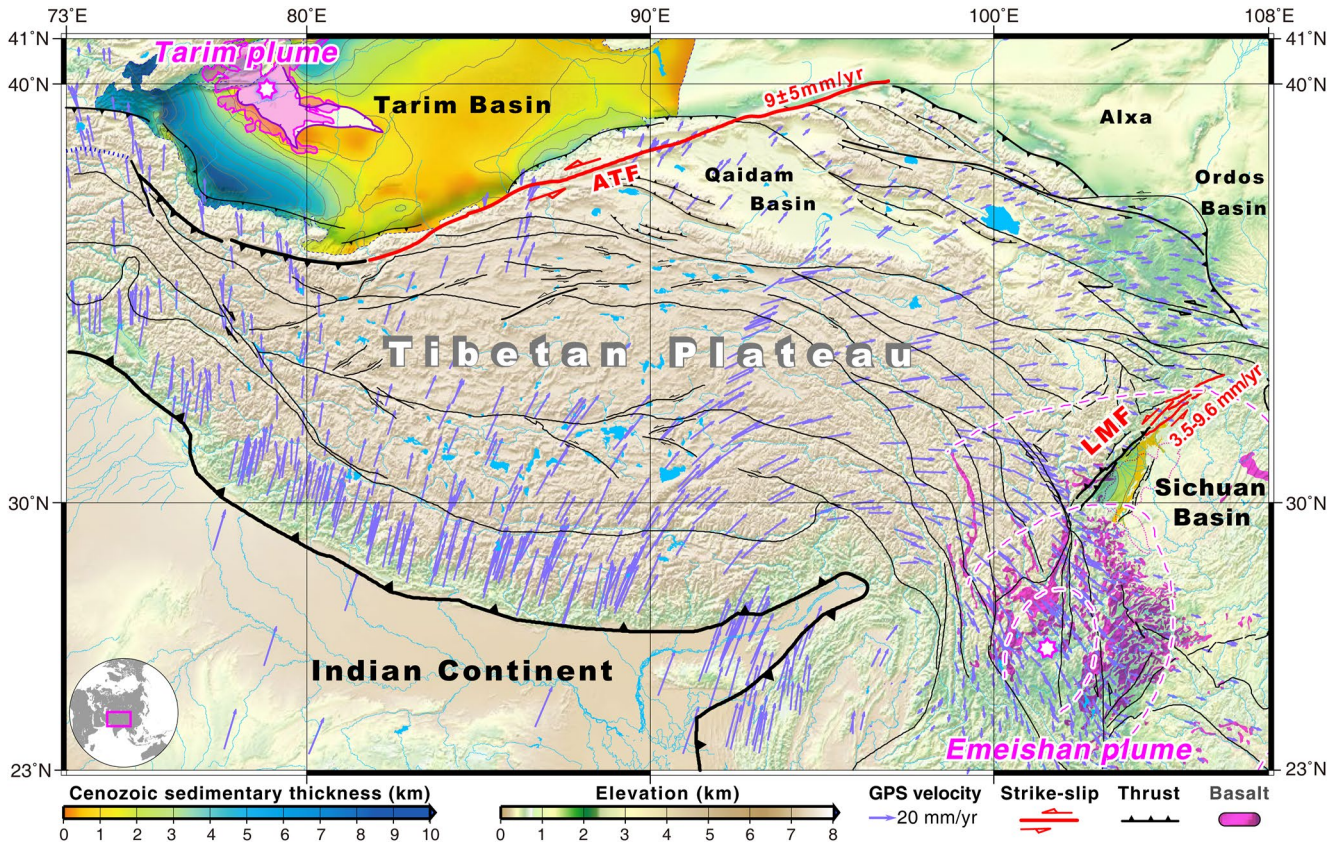

Figure 11. Mode of crustal deformation and strain partitioning along the northern and eastern boundaries of Tibetan Plateau. Pink arrows symbolize direction of the crustal growth of the Tibetan Plateau. Rates of relative motion along the margins of the Tibetan Plateau are from Bendick et al. (2000) and Jiang et al. (2019). The thickness of Cenozoic basin deposits in the northwestern Sichuan Basin and exposed basalts across the southwestern Tibetan Plateau are from Jiang et al. (2019) and Y. Liu et al. (2021), respectively. The pink stars indicate the center of plume head (Y. Chen et al., 2015; X. Xu et al., 2021). The pink-white curves represent the domain of Emeishan plume-driven crustal modification (Y. Chen et al., 2015). ATF, Altyn Tagh fault; LMF, Longmenshan fault.

exposed across the southeastern Tibetan Plateau and Sichuan Basin (Figure 11). Geophysical surveys reveal that the lower crust exhibits densities and fast Vp velocities interpreted to have been caused by plume-related mafic intrusion and underplating (Y. Chen et al., 2015; Y. Liu et al., 2021). The impact of this plume event diminishes to the north. The enrichment of mafic materials in the lower crust would greatly strengthen the lower crust relative to the mid-upper crust (Y. Chen et al., 2015; X. Xu et al., 2021), thus promoting rheologic heterogeneities within the foreland crustal column. Based on our analysis from around the Tarim Basin, we suggest that these heterogeneities caused crustal decoupling to drive upper-crust shortening in the southern Longmen Shan and foreland loading for basin deposition. The northern Longmen Shan did not experience such lower-crustal strengthening, and transcrustal strike-slip faulting cut through the more homogenous crustal column. In this case, the southern region with a mechanically rigid lower crust results in thrust-related shortening, whereas the more homogenous foreland crust to the north results in strike-slip faulting (Figure 11). The similarities of the Longmen Shan and to the orogens around the Tarim Basin confirms the role of the lower-crust rheology in modulating strain partitioning in intra-plate settings.

6. Conclusion

In this work, we have summarized available geologic and geophysical observations around the Tarim Basin, central Asia, including new aeromagnetic, sediment thickness, and gravity maps and seismic-reflection profiles, to assess the variable modes of intra-continental deformation around the relatively undeformed Tarim lithosphere. We observe a distinct difference in deformation, with circum-Tarim Basin thrust belts in the west and predominately strike-slip fault systems around the eastern Tarim Basin. These different deformational modes between western and eastern Tarim Basin may be explained by several potential drivers, including variations in

crustal thickness, pre-Cenozoic geologic histories, and lateral boundary conditions. Our results show that the dichotomy corresponds best to similar differences in aeromagnetic anomalies, where there are strong crustal anomalies in the western Tarim Basin and less prevalent anomalies in the east. We interpret that these differences reflect different compositions of the mid and lower crust, such that the western Tarim Basin may have a more mafic mid-lower crust than the eastern Tarim Basin. These differences probably originated from the Permian Tarim plume, which impacted the western Tarim Basin.

We argue that crustal rheology controls intra-crustal detachments and the mode of intra-continental deformation and strain partitioning. A mafic and mechanically-strong lower crust acts like a rigid underplating block during intra-continental orogeny, where the upper crust easily becomes detached to slide and develop a thrust-dominated belt. Conversely, a crustal column that is not enriched in a mafic lower crust is more vertically homogenous, which promotes a strongly-coupled crustal column that favors localized deformation and strike-slip faulting. Comparative analysis with the Longmen Shan orogen in the eastern Tibetan plateau supports the broad applicability of our model suggesting lower-crust rheology modulates strain portioning in intra-plate settings. Our results can help interpret other intra-plate orogens where strain is complexly partitioned between thrust and strike-slip faulting.

Data Availability Statement

The GPS, magnetic and gravity data are available through Sandwell et al. (2014), X. Xu et al. (2023), and Zheng et al. (2017), respectively. The Cenozoic sediment thickness data is provided in Figure 2c. The seismic reflection data are provided in Figures 4a, 4b, and 5. The other data presented in this study are available in Supporting Information S1.

Acknowledgments
We thank Dr. Lin Chen and Dr. Minqi Liu for useful discussion in lower-crustal rheology, Dr. Hongxiang Wu for sincere help in seismic-reflection interpretation. This research was supported by the Second Tibetan Plateau Scientific Expedition and Research (Grant 2019QZKK00708), the National Natural Science Foundation of China (Grants 41902202 and 42072233), the U.S. National Science Foundation (Grant 1914501), the China Postdoctoral Science Foundation (Grant 2019M652062), and the Geological Survey Project of China (Grants DD20211396 and DD20221715).

References

Authemayou, C., Chardon, D., Bellier, O., Malekzadeh, Z., Shabanian, E., & Abbassi, M. R. (2006). Late Cenozoic partitioning of oblique plate convergence in the Zagros fold-and-thrust belt (Iran). *Tectonics*, *25*(3), 1–21. https://doi.org/10.1029/2005tc001860

Avouac, J. P., & Tapponnier, P. (1993). Kinematic model of active deformation in central Asia. *Geophysical Research Letters*, *20*(10), 895–898. https://doi.org/10.1029/93gl00128

Bao, X., Sun, X., Xu, M., Eaton, D. W., Song, X., Wang, L., et al. (2015). Two crustal low-velocity channels beneath SE Tibet revealed by joint inversion of Rayleigh wave dispersion and receiver functions. *Earth and Planetary Science Letters*, *415*, 16–24. https://doi.org/10.1016/j.epsl.2015.01.020

Bendick, R., Bilham, R., Freymueller, J., Larson, K., & Yin, G. (2000). Geodetic evidence for a low slip rate in the Altyn Tagh fault system. *Nature*, *404*(6773), 69–72. https://doi.org/10.1038/35003555

Bendick, R., & Flesch, L. (2007). Reconciling lithospheric deformation and lower crustal flow beneath central Tibet. *Geology*, *35*(10), 895–898. https://doi.org/10.1130/g23714a.1

Brace, W. F., & Kohlstedt, D. L. (1980). Limits on lithospheric stress imposed by laboratory experiments. *Journal of Geophysical Research*, *85*(B11), 6248–6252. https://doi.org/10.1029/jb085ib11p06248

Brown, E. T., Bendick, R., Bourles, D. L., Gaur, V., Molnar, P., Raisbeck, G. M., & Yiou, F. (2002). Slip rates of the Karakorum fault, Ladakh, India, determined using cosmic ray exposure dating of debris flows and moraines. *Journal of Geophysical Research*, *107*(B9), 1–7. https://doi.org/10.1029/2000jb000100

Burchfiel, B. C., Quidong, D., Molnar, P., Royden, L., Yipeng, W., Peizhen, Z., & Weiqi, Z. (1989). Intracrustal detachment within zones of continental deformation. *Geology*, *17*(8), 748–752. https://doi.org/10.1130/0091-7613(1989)017<0448:idwzoc>2.3.co;2

Bürgmann, R., & Dresen, G. (2008). Rheology of the lower crust and upper mantle: Evidence from rock mechanics, geodesy, and field observations. *Annual Review of Earth and Planetary Sciences*, *36*(1), 531–567. https://doi.org/10.1146/annurev.earth.36.031207.124326

Calignano, E., Sokoutis, D., Willingshofer, E., Gueydan, F., & Cloetingh, S. (2015). Strain localization at the margins of strong lithospheric domains: Insights from analog models. *Tectonics*, *34*(3), 396–412. https://doi.org/10.1002/2014tc003756

Campbell, D. L. (1978). Investigation of the stress-concentration mechanism for intraplate earthquakes. *Geophysical Research Letters*, *5*(6), 477–479. https://doi.org/10.1029/gl005i006p00477

Carroll, A. R., Graham, S. A., Chang, E. Z., & Mcknight, C. (2001). Sinian through Permian tectonostratigraphic evolution of the northwestern Tarim Basin, China. *Geological Society of America Memoirs*, *194*, 47–69.

Chen, H., Lin, X., Cheng, X., Gong, J., Bian, S., Wu, L., et al. (2022). Two-phase intracontinental deformation mode in the context of India–Eurasia collision: Insights from a structural analysis of the West Kunlun–Southern Junggar transect along the NW margin of the Tibetan Plateau. *Journal of the Geological Society*, *179*(2), 1–14. https://doi.org/10.1144/jgs2021-029

Chen, L., Lu, L., Zhu, H., Chen, Y., Huang, Y., Li, Y., & Wang, L. (2017). Improved ethanol electrooxidation performance by shortening Pd–Ni active site distance in Pd–Ni–P nanocatalysts. *Nature Communications*, *8*(1), 1–9. https://doi.org/10.1038/ncomms14136

Chen, W. P., & Molnar, P. (1983). Focal depths of intracontinental and intraplate earthquakes and their implications for the thermal and mechanical properties of the lithosphere. *Journal of Geophysical Research*, *88*(B5), 4183–4214. https://doi.org/10.1029/jb088ib05p04183

Chen, Y., Xu, Y., Xu, T., Si, S., Liang, X., Tian, X., et al. (2015). Magmatic underplating and crustal growth in the Emeishan Large Igneous Province, SW China, revealed by a passive seismic experiment. *Earth and Planetary Science Letters*, *432*, 103–114. https://doi.org/10.1016/j.epsl.2015.09.048

Cheng, F., Zuza, A. V., Haproff, P. J., Wu, C., Neudorf, C., Chang, H., et al. (2021). Accommodation of India–Asia convergence via strike-slip faulting and block rotation in the Qilian Shan fold–thrust belt, northern margin of the Tibetan Plateau. *Journal of the Geological Society*, *178*(3), 1–15. https://doi.org/10.1144/jgs2020-207

Cobbold, P. R., & Davy, P. H. (1988). Indentation tectonics in nature and experiment. II: Central Asia. *Bulletin of the Geological Institution of the University of Upsala*, *14*, 143–162.

Cowgill, E., Yin, A., Arrowsmith, J. R., Feng, W. X., & Shuanhong, Z. (2004). The Akato Tagh bend along the Altyn Tagh fault, northwest Tibet 1: Smoothing by vertical-axis rotation and the effect of topographic stresses on bend-flanking faults. *Geological Society of America Bulletin*, *116*(11–12), 1423–1442. https://doi.org/10.1130/b25359.1

Cowgill, E., Yin, A. N., Harrison, T. M., & Xiao Feng, W. (2003). Reconstruction of the Altyn Tagh fault based on U-Pb geochronology: Role of back thrusts, mantle sutures, and heterogeneous crustal strength in forming the Tibetan Plateau. *Journal of Geophysical Research*, *108*(B7), 1–26. https://doi.org/10.1029/2002jb002080

Deng, Y., Levandowski, W., & Kusky, T. (2017). Lithospheric density structure beneath the Tarim Basin and surroundings, northwestern China, from the joint inversion of gravity and topography. *Earth and Planetary Science Letters*, *460*, 244–254. https://doi.org/10.1016/j.epsl.2016.10.051

Duvall, A. R., & Clark, M. K. (2010). Dissipation of fast strike-slip faulting within and beyond northeastern Tibet. *Geology*, *38*(3), 223–226. https://doi.org/10.1130/g30711.1

England, P., & Houseman, G. (1986). Finite strain calculations of continental deformation: 2. Comparison with the India-Asia collision zone. *Journal of Geophysical Research*, *91*(B3), 3664–3676. https://doi.org/10.1029/jb091ib03p03664

England, P., & Molnar, P. (1990). Right-lateral shear and rotation as the explanation for strike-slip faulting in eastern Tibet. *Nature*, *344*(6262), 140–142. https://doi.org/10.1038/344140a0

Gao, S., Cowgill, E., Wu, L., Lin, X., Cheng, X., Yang, R., et al. (2022). From left slip to transpression: Cenozoic tectonic evolution of the North Altyn fault, NW margin of the Tibetan Plateau. *Tectonics*, *41*(3), e2021T–e6962T. https://doi.org/10.1029/2021tc006962

Geosoft. (2021). Oasis montaj: July 21, 2021 release (Version 9.10) [Software]. Seequent. Retrieved from https://www.seequent.com/oasis-montaj-9-10-release-highlights/

Goetze, C., & Evans, B. (1979). Stress and temperature in the bending lithosphere as constrained by experimental rock mechanics. *Geophysical Journal International*, *59*(3), 463–478. https://doi.org/10.1111/j.1365-246x.1979.tb02567.x

Grant, F. S. (1985). Aeromagnetics, geology and ore environments, I. Magnetite in igneous, sedimentary and metamorphic rocks: An overview. *Geoexploration*, *23*(3), 303–333. https://doi.org/10.1016/0016-7142(85)90001-8

Guo, Z., Yin, A., Robinson, A., & Jia, C. (2005). Geochronology and geochemistry of deep-drill-core samples from the basement of the central Tarim Basin. *Journal of Asian Earth Sciences*, *25*(1), 45–56. https://doi.org/10.1016/j.jseaes.2004.01.016

Hopper, J. R., & Roger Buck, W. (1998). Styles of extensional decoupling. *Geology*, *26*(8), 699–702. https://doi.org/10.1130/0091-7613(1998)026<0699:soed>2.3.co;2

Hu, M., Yu, P., Rao, C., Zhao, C., & Zhang, L. (2019). 3D sharp-boundary inversion of potential-field data with an adjustable exponential stabilizing functional. *Geophysics*, *84*(4), J1–J15. https://doi.org/10.1190/geo2018-0132.1

Jiang, X., Li, Z. X., Li, C., & Gong, W. (2019). A gravity study of the Longmenshan Fault Zone: New insights into the nature and evolution of the fault zone and extrusion-style growth of the Tibetan Plateau since 40 Ma. *Tectonics*, *38*(1), 176–189. https://doi.org/10.1029/2018tc005272

Kusky, T., & Mooney, W. (2015). Is the Ordos Basin floored by a trapped oceanic plateau? *Earth and Planetary Science Letters*, *429*, 197–204. https://doi.org/10.1016/j.epsl.2015.07.069

Laborde, A., Barrier, L., Simoes, M., Li, H., Coudroy, T., Van der Woerd, J., & Tapponnier, P. (2019). Cenozoic deformation of the Tarim Basin and surrounding ranges (Xinjiang, China): A regional overview. *Earth-Science Reviews*, *197*, 102891. https://doi.org/10.1016/j.earscirev.2019.102891

Liu, S., Lei, X., & Wang, L. (2015). New heat flow determination in northern Tarim Craton, northwest China. *Geophysical Journal International*, *200*(2), 1196–1206. https://doi.org/10.1093/gji/ggu458

Liu, Y., Li, L., van Wijk, J., Li, A., & Fu, Y. V. (2021). Surface-wave tomography of the Emeishan large igneous province (China): Magma storage system, hidden hotspot track, and its impact on the Capitanian mass extinction. *Geology*, *49*(9), 1032–1037. https://doi.org/10.1130/g49055.1

Maus, S., Barckhausen, U., Berkenbosch, H., Bournas, N., Brozena, J., Childers, V., et al. (2009). EMAG2: A 2–arc min resolution Earth magnetic anomaly grid compiled from satellite, airborne, and marine magnetic measurements [Dataset]. Geochemistry, Geophysics, Geosystems, *10*(8), 1–12. https://doi.org/10.1029/2009gc002471. Retrieved from http://geomag.org/models/EMAG2

Meade, B. J., & Hager, B. H. (2005). Block models of crustal motion in southern California constrained by GPS measurements. *Journal of Geophysical Research*, *110*(B3), B03403. https://doi.org/10.1029/2004jb003209

Molnar, P., Burchfiel, B. C., K'Uangyi, L., & Ziyun, Z. (1987). Geomorphic evidence for active faulting in the Altyn Tagh and northern Tibet and qualitative estimates of its contribution to the convergence of India and Eurasia. *Geology*, *15*(3), 249–253. https://doi.org/10.1130/0091-7613(1987)15<249:gefafi>2.0.co;2

Molnar, P., England, P., & Martinod, J. (1993). Mantle dynamics, uplift of the Tibetan Plateau, and the Indian monsoon. *Reviews of Geophysics*, *31*(4), 357–396. https://doi.org/10.1029/93rg02030

Molnar, P., & Tapponnier, P. (1975). Cenozoic tectonics of Asia: Effects of a continental collision: Features of recent continental tectonics in Asia can be interpreted as results of the India-Eurasia collision. *Science*, *189*(4201), 419–426. https://doi.org/10.1126/science.189.4201.419

Morgan, J. P., & Vannucchi, P. (2022). Transmogrification of ocean into continent: Implications for continental evolution. *Proceedings of the National Academy of Sciences*, *119*(15), e2122694119. https://doi.org/10.1073/pnas.2122694119

Mouthereau, F., Watts, A. B., & Burov, E. (2013). Structure of orogenic belts controlled by lithosphere age. *Nature Geoscience*, *6*(9), 785–789. https://doi.org/10.1038/ngeo1902

Murphy, M. A., Taylor, M. H., Gosse, J., Silver, C., Whipp, D. M., & Beaumont, C. (2014). Limit of strain partitioning in the Himalaya marked by large earthquakes in western Nepal. *Nature Geoscience*, *7*(1), 38–42. https://doi.org/10.1038/ngeo2017

Qiu, H., Deng, S., Zhang, J., Lin, H., Huang, C., Han, J., et al. (2022). The evolution of a strike-slip fault network in the Guchengxu High, Tarim Basin (NW China). *Marine and Petroleum Geology*, *140*, 105655. https://doi.org/10.1016/j.marpetgeo.2022.105655

Royden, L. (1996). Coupling and decoupling of crust and mantle in convergent orogens: Implications for strain partitioning in the crust. *Journal of Geophysical Research*, *101*(B8), 17679–17705. https://doi.org/10.1029/96jb00951

Saltus, R. W., Hudson, T. L., & Connard, G. G. (1999). A new magnetic view of Alaska. *Geological Society of America Today*, *9*(3), 1–6.

Saltus, R. W., Potter, C. J., & Phillips, J. D. (2006). Crustal insights from gravity and aeromagnetic analysis: Central North Slope, Alaska. *AAPG Bulletin*, *90*(10), 1495–1517. https://doi.org/10.1306/05090605066

Sandwell, D. T., Müller, R. D., Smith, W. H., Garcia, E., & Francis, R. (2014). New global marine gravity model from CryoSat-2 and Jason-1 reveals buried tectonic structure [Dataset]. Science, *346*(6205), 65–67. https://doi.org/10.1126/science.1258213

Schellart, W. P., Chen, Z., Strak, V., Duarte, J. C., & Rosas, F. M. (2019). Pacific subduction control on Asian continental deformation including Tibetan extension and eastward extrusion tectonics. *Nature Communications*, *10*(1), 4480. https://doi.org/10.1038/s41467-019-12337-9

Shen, Z., Sun, J., Zhang, P., Wan, Y., Wang, M., Bürgmann, R., et al. (2009). Slip maxima at fault junctions and rupturing of barriers during the 2008 Wenchuan earthquake. *Nature Geoscience*, *2*(10), 718–724. https://doi.org/10.1038/ngeo636
Skeels, D. C. (1967). What is residual gravity? *Geophysics*, *32*(5), 872–876. https://doi.org/10.1190/1.1439896
Tapponnier, P., Peltzer, G. L. D. A. Y., Le Dain, A. Y., Armijo, R., & Cobbold, P. (1982). Propagating extrusion tectonics in Asia: New insights from simple experiments with plasticine. *Geology*, *10*(12), 611–616. https://doi.org/10.1130/0091-7613(1982)10<611:petian>2.0.co;2
Tian, H., Chen, H., Cheng, X., Wu, L., Lin, X., Gao, S., et al. (2023). Limited northward expansion of the Tibetan Plateau in the late Cenozoic: Insights from the Cherchen fault in the southeastern Tarim Basin. *Tectonics*, *42*(7). Portico. https://doi.org/10.1029/2022tc007694
Tian, X., Bai, Z., Klemperer, S. L., Liang, X., Liu, Z., Wang, X., et al. (2021). Crustal-scale wedge tectonics at the narrow boundary between the Tibetan Plateau and Ordos block. *Earth and Planetary Science Letters*, *554*, 116700. https://doi.org/10.1016/j.epsl.2020.116700
Wang, Q. W., Kan, Z. Z., Liang, B., & Zeng, Y. J. (2006). Stratigraphic division and correlation of the continental Meso-Cenozoic group in Ya'an [in Chinese with English abstract]: West Sichuan Basin. *Acta Geologica Sichuan*, *26*(2), 65–69.
Wen, B., Evans, D. A., Wang, C., Li, Y., & Jing, X. (2018). A positive test for the Greater Tarim Block at the heart of Rodinia: Mega-dextral suturing of supercontinent assembly. *Geology*, *46*(8), 687–690. https://doi.org/10.1130/g40254.1
Windley, B. F., Allen, M. B., Zhang, C., Zhao, Z. Y., & Wang, G. R. (1990). Paleozoic accretion and Cenozoic redeformation of the Chinese Tien Shan range, central Asia. *Geology*, *18*(2), 128–131. https://doi.org/10.1130/0091-7613(1990)018<0128:paacro>2.3.co;2
Wu, C., Yin, A., Zuza, A. V., Zhang, J., Liu, W., & Ding, L. (2016). Pre-Cenozoic geologic history of the central and northern Tibetan Plateau and the role of Wilson cycles in constructing the Tethyan orogenic system. *Lithosphere*, *8*(3), 254–292. https://doi.org/10.1130/l494.1
Wu, G., Yang, S., Meert, J. G., Xiao, Y., Chen, Y., Wang, Z., & Li, X. (2020). Two phases of Paleoproterozoic orogenesis in the Tarim Craton: Implications for Columbia assembly. *Gondwana Research*, *83*, 201–216. https://doi.org/10.1016/j.gr.2020.02.009
Wu, L., Lin, X., Cowgill, E., Xiao, A., Cheng, X., Chen, H., et al. (2019). Middle Miocene reorganization of the Altyn Tagh fault system, northern Tibetan Plateau. *GSA Bulletin*, *131*(7–8), 1157–1178. https://doi.org/10.1130/b31875.1
Xiao, W., Windley, B. F., Allen, M. B., & Han, C. (2013). Paleozoic multiple accretionary and collisional tectonics of the Chinese Tianshan orogenic collage. *Gondwana Research*, *23*(4), 1316–1341. https://doi.org/10.1016/j.gr.2012.01.012
Xiao, W., Windley, B. F., Hao, J., & Zhai, M. (2003). Accretion leading to collision and the Permian Solonker suture, Inner Mongolia, China: Termination of the central Asian orogenic belt. *Tectonics*, *22*(6), 1–20. https://doi.org/10.1029/2002tc001484
Xiong, S., Yang, H., Ding, Y., Li, Z., & Li, W. (2016). Distribution of igneous rocks in China revealed by aeromagnetic data. *Journal of Asian Earth Sciences*, *129*, 231–242. https://doi.org/10.1016/j.jseaes.2016.08.016
Xu, X., Chen, H., Zuza, V. A., Yin, A., Yu, P., Lin, X., et al. (2023). Phanerozoic cratonization by plume welding. *Geology*, *51*(2), 209–214. https://doi.org/10.1130/g050615.1
Xu, X., Zuza, A. V., Yin, A., Lin, X., Chen, H., & Yang, S. (2021). Permian plume-strengthened Tarim lithosphere controls the Cenozoic deformation pattern of the Himalayan-Tibetan orogen. *Geology*, *49*(1), 96–100. https://doi.org/10.1130/g47961.1
Xu, Y., Liu, F., Liu, J., & Chen, H. (2002). Crust and upper mantle structure beneath western China from P wave travel time tomography. *Journal of Geophysical Research*, *107*(B10), 1–4. https://doi.org/10.1029/2001jb000402
Xu, Z., He, B., Zhang, C., Zhang, J., Wang, Z., & Cai, Z. (2013). Tectonic framework and crustal evolution of the Precambrian basement of the Tarim Block in NW China: New geochronological evidence from deep drilling samples. *Precambrian Research*, *235*, 150–162. https://doi.org/10.1016/j.precamres.2013.06.001
Yang, H., Wu, G., Kusky, T. M., Chen, Y., & Xiao, Y. (2018). Paleoproterozoic assembly of the North and South Tarim terranes: New insights from deep seismic profiles and Precambrian granite cores. *Precambrian Research*, *305*, 151–165. https://doi.org/10.1016/j.precamres.2017.11.015
Yang, J., Kaus, B. J., Li, Y., Leloup, P. H., Popov, A. A., Lu, G., et al. (2020). Lower crustal rheology controls the development of large offset strike-slip faults during the Himalayan-Tibetan orogeny. *Geophysical Research Letters*, *47*(18), e2020G–e89435G. https://doi.org/10.1029/2020gl089435
Yang, S., Chen, H., Li, Z., Li, Y., Yu, X., Li, D., & Meng, L. (2013). Early Permian Tarim large igneous province in northwest China. *Science China Earth Sciences*, *56*(12), 2015–2026. https://doi.org/10.1007/s11430-013-4653-y
Yin, A. (2010). Cenozoic tectonic evolution of Asia: A preliminary synthesis. *Tectonophysics*, *488*(1–4), 293–325. https://doi.org/10.1016/j.tecto.2009.06.002
Yin, A., & Harrison, T. M. (2000). Geologic evolution of the Himalayan-Tibetan orogen. *Annual Review of Earth and Planetary Sciences*, *28*(1), 211–280. https://doi.org/10.1146/annurev.earth.28.1.211
Yin, A., Nie, S., Craig, P., Harrison, T. M., Ryerson, F. J., Xianglin, Q., & Geng, Y. (1998). Late Cenozoic tectonic evolution of the southern Chinese Tian Shan. *Tectonics*, *17*(1), 1–27. https://doi.org/10.1029/97tc03140
Yin, A., & Nie, S. Y. (1996). 20 A Phanerozoic palinspastic reconstruction of China and its neighboring regions. In *The tectonic evolution of Asia*. Cambridge University.
Yin, A., Rumelhart, P. E., Butler, R., Cowgill, E., Harrison, T. M., Foster, D. A., et al. (2002). Tectonic history of the Altyn Tagh fault system in northern Tibet inferred from Cenozoic sedimentation. *Geological Society of America Bulletin*, *114*(10), 1257–1295. https://doi.org/10.1130/0016-7606(2002)114<1257:thotat>2.0.co;2
Yin, A., & Taylor, M. H. (2011). Mechanics of V-shaped conjugate strike-slip faults and the corresponding continuum mode of continental deformation. *Geological Society of America Bulletin*, *123*(9–10), 1798–1821. https://doi.org/10.1130/b30159.1
Zhang, C., Zou, H., Li, H., & Wang, H. (2013). Tectonic framework and evolution of the Tarim Block in NW China. *Gondwana Research*, *23*(4), 1306–1315. https://doi.org/10.1016/j.gr.2012.05.009
Zhao, J., Mooney, W. D., Zhang, X., Li, Z., Jin, Z., & Okaya, N. (2006). Crustal structure across the Altyn Tagh Range at the northern margin of the Tibetan Plateau and tectonic implications. *Earth and Planetary Science Letters*, *241*(3–4), 804–814. https://doi.org/10.1016/j.epsl.2005.11.003
Zhao, P., He, J., Deng, C., Chen, Y., & Mitchell, R. N. (2021). Early Neoproterozoic (870–820 Ma) amalgamation of the Tarim craton (northwestern China) and the final assembly of Rodinia. *Geology*, *49*(11), 1277–1282. https://doi.org/10.1130/g48837.1
Zheng, G., Wang, H., Wright, T. J., Lou, Y., Zhang, R., Zhang, W., et al. (2017). Crustal deformation in the India-Eurasia collision zone from 25 years of GPS measurements. *Journal of Geophysical Research: Solid Earth*, *122*(11), 9290–9312. https://doi.org/10.1002/2017jb014465
Zuza, A. V., Wu, C., Reith, R. C., Yin, A., Li, J., Zhang, J., et al. (2018). Tectonic evolution of the Qilian Shan: An early Paleozoic orogen reactivated in the Cenozoic. *GSA Bulletin*, *130*(5–6), 881–925. https://doi.org/10.1130/b31721.1
Zuza, A. V., & Yin, A. (2016). Continental deformation accommodated by non-rigid passive bookshelf faulting: An example from the Cenozoic tectonic development of northern Tibet. *Tectonophysics*, *677–678*, 227–240. https://doi.org/10.1016/j.tecto.2016.04.007
Zuza, A. V., & Yin, A. (2017). Balkatach hypothesis: A new model for the evolution of the Pacific, Tethyan, and Paleo-Asian oceanic domains. *Geosphere*, *13*(5), 1664–1712. https://doi.org/10.1130/ges01463.1

References From the Supporting Information

Gao, R., Huang, D., Lu, D., Qian, G., Li, Y., Kuang, C., et al. (2000). Deep seismic reflection profile across the juncture zone between the Tarim Basin and the West Kunlun Mountains. *Chinese Science Bulletin*, *45*(24), 2281–2286. https://doi.org/10.1007/bf02886369

Gilligan, A., Priestley, K. F., Roecker, S. W., Levin, V., & Rai, S. S. (2015). The crustal structure of the western Himalayas and Tibet. *Journal of Geophysical Research: Solid Earth*, *120*(5), 3946–3964. https://doi.org/10.1002/2015jb011891

Huang, J., & Zhao, D. (2006). High-resolution mantle tomography of China and surrounding regions. *Journal of Geophysical Research*, *111*(B9), B09305. https://doi.org/10.1029/2005jb004066

Li, C., Van der Hilst, R. D., Meltzer, A. S., & Engdahl, E. R. (2008). Subduction of the Indian lithosphere beneath the Tibetan Plateau and Burma. *Earth and Planetary Science Letters*, *274*(1–2), 157–168. https://doi.org/10.1016/j.epsl.2008.07.016

Li, J., Zhang, J., Zhao, X., Jiang, M., Li, Y., Zhu, Z., et al. (2016). Mantle subduction and uplift of intracontinental mountains: A case study from the Chinese Tianshan Mountains within Eurasia. *Scientific Reports*, *6*(1), 1–8. https://doi.org/10.1038/srep28831

Rai, S. S., Priestley, K., Gaur, V. K., Mitra, S., Singh, M. P., & Searle, M. (2006). Configuration of the Indian Moho beneath the NW Himalaya and Ladakh. *Geophysical Research Letters*, *33*(15), L15308. https://doi.org/10.1029/2006gl026076

Tunini, L., Jiménez-Munt, I., Fernandez, M., Vergés, J., Villaseñor, A., Melchiorre, M., & Afonso, J. C. (2016). Geophysical-petrological model of the crust and upper mantle in the India-Eurasia collision zone. *Tectonics*, *35*(7), 1642–1669. https://doi.org/10.1002/2016tc004161

Wittlinger, G., Tapponnier, P., Poupinet, G., Mei, J., Danian, S., Herquel, G., & Masson, F. (1998). Tomographic evidence for localized lithospheric shear along the Altyn Tagh fault. *Science*, *282*(5386), 74–76. https://doi.org/10.1126/science.282.5386.74

Wittlinger, G., Vergne, J., Tapponnier, P., Farra, V., Poupinet, G., Jiang, M., et al. (2004). Teleseismic imaging of subducting lithosphere and Moho offsets beneath western Tibet. *Earth and Planetary Science Letters*, *221*(1–4), 117–130. https://doi.org/10.1016/s0012-821x(03)00723-4

Zhao, J., Yuan, X., Liu, H., Kumar, P., Pei, S., Kind, R., et al. (2010). The boundary between the Indian and Asian tectonic plates below Tibet. *Proceedings of the National Academy of Sciences*, *107*(25), 11229–11233. https://doi.org/10.1073/pnas.1001921107